LA-14235
Approved for public release;
distribution is unlimited.

Phase-Space Density Analyses of the AE-8 Trapped Electron and the AP-8 Trapped Proton Model Environments

Thomas E. Cayton

The World's Greatest Science Protecting America

LA-14235
Approved for public release;
distribution is unlimited.

Phase-Space Density Analyses of the AE-8 Trapped Electron and the AP-8 Trapped Proton Model Environments

Thomas E. Cayton

The World's Greatest Science Protecting America

Table of Contents

Phase-Space Density Analyses of the AE-8 Trapped Electron and the AP-8 Trapped Proton Model Environments

by

Thomas E. Cayton

Abstract

The AE-8 trapped electron and the AP-8 trapped proton models are used to examine the L-shell variation of phase-space densities for sets of transverse (or 1st) invariants, μ, and geometrical invariants, K (related to the first two adiabatic invariants). The motivation for this study is twofold: first, to discover the functional dependence of the phase-space density upon the invariants; and, second, to explore the global structure of the radiation belts within this context. Variation due to particle rest mass is considered as well. The overall goal of this work is to provide a framework for analyzing energetic particle data collected by instruments on Global Positioning System (GPS) spacecraft that fly through the most intense region of the radiation belt.

For all considered values of μ and K, and for $3.5\ R_E < L < 6.5\ R_E$, the AE-8 electron phase-space density increases with increasing L; this trend—the expected one for a population diffusing inward from an external source—continues to $L = 7.5\ R_E$ for both small and large values of K but reverses slightly for intermediate values of K. The AP-8 proton phase-space density exhibits μ-dependent local minima around $L = 5\ R_E$. Both AE-8 and AP-8 exhibit critical or cutoff values for the invariants beyond which the flux and therefore the phase-space density vanish. For both electrons and protons, these cutoff values vary systematically with magnetic moment and L-shell and are smaller than those estimated for the atmospheric loss cone. For large magnetic moments, for both electrons and protons, the K-dependence of the phase-space density is exponential, with maxima at the magnetic equator ($K = 0$) and vanishing beyond a cutoff value, K_c. Such features suggest that momentum-dependent trapping boundaries, perhaps drift-type loss cones, serve as boundary conditions for trapped electrons as well as trapped protons.

---

1. Introduction

The AE-8 Trapped Electron Model Environment[1] and the AP-8 Trapped Proton Model Environment[2] provide global estimates for omnidirectional integral fluxes of energetic particles trapped in the earth's geomagnetic field for a given particle energy and position in the magnetosphere, parameterized in terms of L-shell and the ratio, B/B_0, of the magnetic field intensity at the observation point to its minimum value on the same field line. These empirical models incorporate experimental results from many different instruments and

investigators and represent the latest generation of a family of such empirical models with a legacy of nearly four decades.[3-9]

AP-8 combined measurements from 94 instrument channels that flew on 24 different spacecraft through a broad range of altitudes and inclinations, from 300-km polar orbits, to geostationary orbits, to highly elliptical inclined and equatorial orbits.[2] AE-8 supplemented the measurements of electron flux from the 1960s through the mid-1970s with new data from five satellites, OV1-19, OV3-3, Azur, ATS-5, and ATS-6.[1] These models return flux above a set of threshold energies, similar to the actual output of energetic particle instruments;[10] indeed, the models are essentially flux maps derived from integral- and differential-fluxes measured across the ranges of energies, L-shells, and mirror points of interest, with interpolated values between the measured values. Differencing the integral fluxes associated with adjacent thresholds provides estimates of the differential particle fluxes.

Although the primary use of these models has been to provide quantitative estimates for radiation damage, shielding requirements, orbit selection, and mission lifetime estimation, they also provide a reasonable picture of the global spatial distribution of the trapped particle population that may guide theoretical notions and concepts. While these empirical models have been characterized as being both too low[11] and too high,[12] some model predictions have been found to agree well with measurements.[13,14] The uncertainties in the models are greatest in regions that exhibit steep spatial or spectral gradients or where the time-dependence is dominated by rare, but large, events (i.e., events not well characterized by a time average).

Here, the models will be evaluated in a particular fashion to examine the L-shell variation of phase-space densities for sets of transverse invariants, μ, and geometrical invariants, K, as well as particle rest mass, m_e and m_p, implied by the separate electron and proton models. The goal of this work is to provide some context for analysis of energetic particle data collected by the Burst Detection Dosimeter (BDD) and the Combined X-ray Sensor and Dosimeter (CXD) instruments on GPS satellites. The following points summarize the results of these analyses:

(1) For all considered values of μ and K, and for $3.5\ R_E < L < 6.5\ R_E$, the AE-8 electron phase-space density *increases* with increasing L—the expected trend for a population diffusing inward from an external source.

(2) For both small and large values of K, the AE-8 phase-space density continues to increase with increasing L out to at least $7.5\ R_E$.

(3) For intermediate values of K, and $6.5\ R_E < L < 7.5\ R_E$, the AE-8 electron phase-space density decreases slightly with increasing L.

(4) In the outer region, $5.5\ R_E < L < 7.5\ R_E$, the L- gradient of the AE-8 electron phase-space density is much weaker than in the inner region.

(5) The AP-8 proton phase-space density exhibits μ-dependent local minima around $L = 5\ R_E$. This suggests populations diffusing both outward from an internal source and inward from an external source toward a lossy central region near $L = 5\ R_E$.

(6) For large magnetic moments—for both electrons and protons—the K-dependence of the phase-space density is exponential, with maxima at the magnetic equator (K = 0), and vanishing beyond a cutoff value, K_c.

(7) The cutoff values, K_c, vary systematically with μ and L-shell and are smaller than those estimated for the atmospheric loss cone; for small μ, the K_c values approach those of the atmospheric loss cone.

The rest of this paper is organized as follows: Section 2 presents the method of analysis, the parameters, and the sets of values used. Sections 3 and 4 present the results. Section 5 applies general features of the AP-8 phase-space analysis to a discussion of trapped proton data measured at GPS orbits. Section 6 presents a summary and draws conclusions.

2. Analysis

The AE-8 and AP-8 models were evaluated for the following nine L-shell values, in the units R_E:

$$L = \{3.5, 4.0, 4.5, 5.0, 5.5, 6.0, 6.5, 7.0, 7.5\}. \quad (1)$$

A dipole magnetic field was assumed, and the IGRF2005 value was used for the dipole moment. The magnetic field at the magnetic equator, B_0, therefore, is given in G by

$$B_0 = 0.30036/L^3. \quad (2)$$

Two different sets of mirror point fields were evaluated from specified values of the geometrical invariant, K, in units of $G^{1/2}$-R_E.

$$K \equiv \int_{-s_m}^{s_m} \left[B_m - B(s)\right]^{1/2} ds = J / (8 m_0 \mu)^{1/2}, \quad (3)$$

where the integration path follows a field line between mirror points, $B(s_m) = B_m$, and μ and J are the first and second adiabatic invariants, respectively, for a particle of rest mass m_0 (m_e for electrons, or m_p for protons), gyrating and bouncing between the mirror points. For a dipole field, an approximation by Chen and Stern[15] yields the ratio B_m/B_0 from specified values of L and K. In terms of the dimensionless variable $X = K/(L\, B_0^{1/2})$, the ratio is[16]

$$B_m/B_0 = 1 + 1.35048\, X - 0.030425\, X^{4/3} + 0.10066\, X^{5/3} + 0.13124203\, X^2. \quad (4)$$

The AE-8 and AP-8 models were evaluated for two sets of values for the geometrical invariant, K—a small set of 12 values and a large set of 161 values. In the units $G^{1/2}$-R_E, the small set is

$$K = \{0.0000, 0.0012, 0.0048\ 0.0200, 0.0492, 0.1000, 0.1919, 0.3670, 0.7690, 1.2090, 2.1380, 5.070\}. \quad (5)$$

The equatorial pitch angles, α_0, corresponding to this set vary with L-shell. For example, at $L = 3.5\ R_E$, the set of pitch angles (in degrees) corresponding to Eq. (5) is

$$\alpha_0(3.5) = \{90.00, 85.75, 81.54, 75.03, 64.24, 55.12, 45.39, 35.24, 24.44, 18.75, 12.86, 6.68\},$$

while at L = 7.5 R_E,

$$\alpha_0(7.5) = \{90.00, 84.86, 79.79, 69.69, 59.57, 49.54, 39.41, 29.49, 19.59, 14.65, 9.74, 4.86\}.$$

The large set of K values consists of 6 values between 0.000 and 0.005 in linear increments of 0.001, followed by 58 values between 0.010 and 0.295 in linear increments of 0.005, followed by 96 logarithmically spaced values between 0.3020 and 25.1189, in base-10 logarithmic increments of 0.02. For each L-shell, Eqs. (4) and (2) provide sets of field line ratios, B_m/B_0, and mirror fields, B_m, corresponding to the specified set of K values.

The particle energies at which the AE-8 and AP-8 fluxes were evaluated were calculated from sets of 31 values of the transverse adiabatic invariant, μ, in the units MeV/G. For electrons the values were logarithmically spaced between 40 and 40,000, in base-10 logarithmic increments of 0.1. For protons, 10 linearly spaced values were chosen between 25 and 250, followed by 21 logarithmically spaced values between 250 and 2672.637, in base-10 logarithmic increments of 0.049. Particles were assumed to mirror *at or above* the mirror field, B_m, and their total momenta and kinetic energies were determined by

$$p^2/2m_0 = \mu B_m = E(1+E/2m_0c^2). \quad (6)$$

(These are the lower limits above which the AE-8 or AP-8 integral fluxes are returned.)

The kinetic energies, therefore, are given by

$$E = m_0c^2 (1 + 2 \mu B_m/m_0c^2)^{1/2} - m_0c^2. \quad (7)$$

For electrons, $m_ec^2 = 0.511$ MeV; for protons, $m_pc^2 = 938.3$ MeV.

Finally, the phase-space density or distribution function was calculated from the models by evaluating at each L-shell, B_m/B_0, and E the differential particle flux and dividing the result by $p^2/2m_0$. The phase-space densities of electrons and protons are given, therefore, in the units particles/(cm^2-s-sr-MeV^2). Differencing integral fluxes returned from the AE-8 or AP-8 model yields the following approximation for the average differential flux in units of particles/(cm^2-s-sr-MeV):

$$dj/dEd\Omega \cong (J(E+\delta) - J(E-\delta))/8\pi\delta. \quad (8)$$

The value 0.1 E was used for δ in these evaluations. Dividing Eq. (8) by Eq. (6) yields the phase-space density in units of particles/(cm^2-s-sr-MeV^2), as stated above.

3. Results: AE-8 Electrons

A. μ-dependence

The electron phase-space density from the AE-8 trapped electron model environment is plotted as functions of μ for the twelve values of K specified by Eq. (5) for a single L-shell in Figs. A1–A18 of Appendix A. The same results are plotted twice for each L-shell specified

by Eq. (1), first in a linear-log (semilog) format and then in a log-log format. [The term "magnetic moment" is here used interchangeably, but incorrectly, with "transverse adiabatic invariant." The two quantities differ by the factor $m_0c^2/(E+m_0c^2)$.]

Several qualitative features of the electron population in the parameter space (μ, K, L) are apparent in Figs. A1–A18, including the following:

(1) On all L-shells and for all μ, the maximum phase-space density occurs on the magnetic equator, where K = 0; the phase-space density decreases monotonically with increasing K.

(2) A trapped population of electrons is not seen everywhere in this parameter space but is limited to specific regions. For larger values of K, the trapped population vanishes above progressively smaller values of μ. In some cases, the region shrinks to zero, and no trapped population occurs within the considered range of parameters, e.g., in Figs. A1 and A2, when $K > 5.07\ G^{1/2}\text{-}R_{E,}$ the phase-space density vanishes for all μ (within the range considered here).

(3) As a function of μ, the *form* of the electron phase-space density varies systematically from the lower L-shells to the higher one. In the inner region, $3.5\ R_E < L < 5.5\ R_E$, a power-law dependence upon μ is apparent for the smaller values (approximately linear small-μ asymptotes in Figs A2, A4, A6, A8, and A10), but the dependence becomes exponential at the larger values (approximately linear large-μ asymptotes in Figs. A1, A3, A5, A7, and A9). Indeed, the three-parameter model of the phase-space density,

$$F(\mu) = A\ \mu^B \exp(-\mu/C), \tag{9}$$

where A, B, and C are parameters, reproduces this variation rather well. (The family of functions given in Eq. (9) has proved useful in modeling various phenomena, from spectra of gamma-ray bursts[17] to the pulse shape observed in active circuits[18]). Beyond $L = 5.5\ R_E$, the phase-space density vanishes more rapidly at large μ than according to the simple exponential form seen in the inner region (*viz.,* the downward curvature in Fig. A13 at large μ). While this may be a real feature of the trapped electron population, it may be an artifact of the interpolation scheme used in the original AE-8 model or an *ad hoc* cutoff in the model. Also in the outer region, another roll-off occurs at small μ near the magnetic equator (smaller K values; *viz.,* the downward curvature in Fig. A14 at small μ). This might be evidence for a saturation of the electron population; it might also be an artifact of extrapolating AE-8 beyond its practical limits.

In any event, simple functional forms, like Eq. (9), fail to reproduce the more complex variation encountered in the outer region; a polynomial (truncated power series) in the logarithm of μ, however, can reproduce this behavior.

$$\log(f(\mu)) = \sum a_n\ (\log(\mu))^n. \tag{10}$$

where $f(\mu)$ is the electron phase-space density, the sum includes values 0 to 3 or 4, and the a_n are constants. Except for the largest K values on the largest L-shells, however, a simple power law [Eq. (10) with coefficients a_0 and a_1 only] is a totally inadequate representation.

B. K-dependence

The electron phase-space density from the AE-8 trapped electron model environment is plotted as functions of K for the nine L-shells specified in Eq. (1) for twelve fixed values of magnetic moment, μ, in Figs. B1–B12 of Appendix B. For clarity, the first panel shows results from the inner region, $3.5\ R_E < L < 5.5 R_E$, and the second panel, results from the outer region, $5.5\ R_E < L < 7.5 R_E$. The large set of 161 K values was used as follows:

For each μ and L-shell, the largest K associated with a finite phase-space density was determined (the phase-space density vanishes for all larger values of K). A cutoff value, K_c, was calculated by averaging the two values corresponding to the last finite and the first zero values of the phase-space density. The K-dependence of the logarithm of the phase-space density was then represented as polynomials in the scaled variable K/K_c:

$$\log(f(K)) = \sum b_n \, (K/K_c)^n. \tag{11}$$

The order of the fitting polynomial varied from 1 to 8, depending on the number of finite values of the phase-space density, 7 to 143.

Several qualitative features of the electron population in the parameter space (μ, K, L) are apparent in Figs. B1–B12, including the following:

(1) For all considered values of μ and K, and for $3.5\ R_E < L < 6.5\ R_E$, the AE-8 electron phase-space density *increases* with increasing L.

(2) For both small and large values of K, the AE-8 phase-space density continues to increase, albeit slowly, with increasing L out to at least $7.5\ R_E$.

(3) For intermediate values of K, and $6.5\ R_E < L < 7.5\ R_E$, the AE-8 electron phase-space density decreases slightly with increasing L.

(4) As a function of K, the form of the electron phase-space density varies systematically with μ and L-shell; no characteristic function, simply multiplied by different amplitudes, is apparent.

(5) For large magnetic moments, the K-dependence of the phase-space density is exponential, with maxima at the magnetic equator (K = 0), and vanishing beyond a cutoff value, K_c.

(6) The cutoff values, K_c, vary systematically with magnetic moment and L-shell and are smaller than those estimated for the atmospheric loss cone.

The cutoff values of the geometrical invariant K are plotted as functions of magnetic moment μ for the nine L-shells specified in Fig. 1.

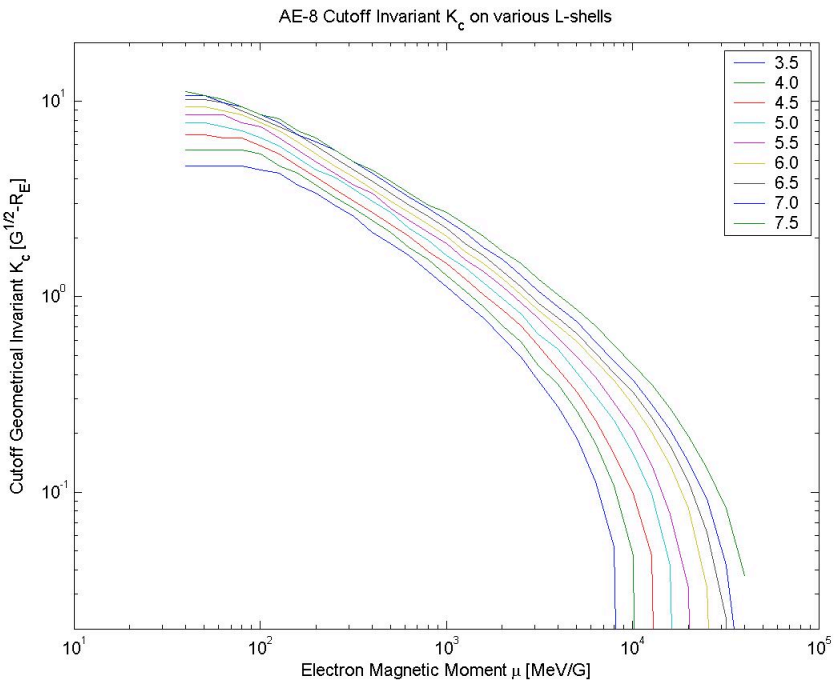

Figure 1. Cutoff invariant K_c as functions of μ on nine L-shells as labeled. AE-8 phase-space density vanishes in the regions above and to the right of the curves.

At low μ the cutoff values approach those estimated for the atmospheric loss cone. Using the IGRF2005 dipole moment and its offset from the dipole axis, 0.0842 R_E , and assuming atmospheric loss at 100 km altitude, one obtains the following set of equatorial pitch angles, α_{ALC} [degrees] and K_{ALC} [$G^{1/2}$-R_E], corresponding to the L-shells given in Eq. (1):

$$\alpha_{ALC} = \{7.21, 5.82, 4.83, 4.09, 3.52, 3.07, 2.71, 2.41, 2.17\}.$$

$$K_{ALC} = \{4.612, 5.618, 6.629, 7.643, 8.659, 9.678, 10.70, 11.72, 12.47\}.$$

The cutoff values, K_c, correspond directly to cutoff values of the equatorial pitch angle, α_c, below which the phase-space density vanishes; these cutoff values of the equatorial pitch angle α are plotted as functions of magnetic moment μ in Fig. 2 for the nine L-shells specified. These two figures suggest that momentum-dependent trapping boundaries, perhaps drift-type loss cones, serve as boundary conditions for the trapped electron population represented in the AE-8 model environment. Here, the term "drift-type loss cone" simply means that the drift shell is open or stochastic rather than closed and laminar and therefore that high-momentum electrons are not stably trapped.

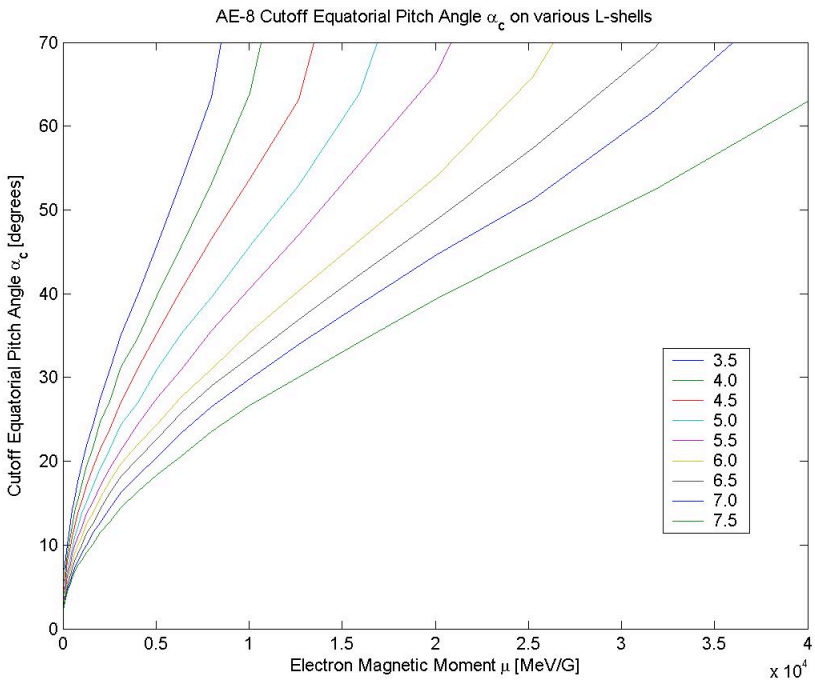

Figure 2. Cutoff equatorial pitch angle α_c as functions of μ on nine L-shells as labeled. AE-8 phase-space density vanishes in the regions below and to the right of the curves.

4. Results: AP-8 Protons

C. μ-dependence

The proton phase-space density from the AP-8 trapped proton model environment is plotted as functions of μ for the twelve values of K specified by Eq. (5) for a single L-shell in Figs. C1–C18 of Appendix C. The same results are plotted twice for each L-shell specified by Eq. (1): first in a linear-log (semilog) format and then in a log-log format. (The results shown for L = 7.5 R_E extrapolate beyond the L-range of AP-8 and should be viewed with caution; likewise, some of the lower μ values extrapolate AP-8 below the intended energy range that begins at 0.1 MeV: μ > 30, 42, 55, 72, 91, and 114 MeV/G for L = 4.5 to 7.0 R_E.)

Several qualitative features of the proton population in the parameter space (μ, K, L) are apparent in Figs. C1–C18, including the following:

(1) On all L-shells and for all μ, the maximum phase-space density occurs on the magnetic equator, where K = 0; as with the AE-8 electrons, the proton phase-space density decreases monotonically with increasing K.

(2) A trapped population of protons, like the electron population, is limited to specific regions. For larger values of K, the trapped population vanishes above progressively smaller values of μ. In some cases, the region shrinks to zero, and no trapped population occurs within the considered range of parameters, e.g., in Figs. C3–C18

there are no curves for K = 2.138 and K = 5.070 $G^{1/2}$-R_E because the phase-space density vanishes for all μ (within the range considered here).

(3) As a function of μ, the *form* of the proton phase-space density varies systematically from the lower L-shells to the higher one. In the inner region, 3.5 R_E < L < 4.5 R_E, a power-law tail is apparent for the larger μ values, but the phase-space density rolls off at smaller μ values. Indeed, the three-parameter model of the phase-space density,

$$F(\mu) = A\,(1 + \mu/B)^{-C}, \tag{12}$$

(where, again, A, B, and C are parameters) reproduces this variation rather well. The family of functions given in Eq. (12) has proved useful in modeling flux spectra of ions and electrons encountered in the plasma sheet.[19] At and beyond L = 5.0 R_E , the AP-8 phase-space density exhibits an exponential tail at large μ values; the form is similar to the one exhibited by electrons in the inner region and represented by Eq. (9).

D. K-dependence

The proton phase-space density from the AP-8 trapped proton model environment is plotted as functions of K for the nine L-shells specified in Eq. (1) for six fixed values of magnetic moment, μ, in Figs. D1–D6 of Appendix D. For clarity, the first panel shows results from the inner region, 3.5 R_E < L < 5.0R_E, and the second panel, results from the outer region, 5.0 R_E < L < 7.5R_E. The large set of 161 K values was used; cutoff values, K_c, were calculated; and polynomial representations in terms of scaled variables, K/K_c [Eq. (11)], were determined for the proton phase-space density (exactly the same approach previously described for electrons). Again, the order of the fitting polynomial varied from 1 to 8, depending on the number of finite values of the phase-space density, 6 to 117.

Within certain restricted ranges of the parameter values L and B/B_0, the AP-8 model returns discontinuous flux profiles. These small discontinuities cause unphysical wiggles in the fitting polynomial, e.g., the line labeled L = 5.0 in Figs. D2a and D2b and the line labeled L = 4.5 in Figs. 3a and 3b. Such features appear to be an artifact from the AP-8 flux maps themselves or of the interpolation scheme that uses them.

Several qualitative features of the proton population in the parameter space (μ, K, L) are apparent in Figs. D1–D6, including the following.

(1) The AP-8 proton phase-space density exhibits μ-dependent local minima around L = 5 R_E. To make this clearer, several L-profiles for fixed values of μ and K will be shown in Subsection E, L-dependence. This suggests populations diffusing both outward from an internal source and inward from an external source toward a lossy central region near L = 5 R_E.

(2) For magnetic moments larger than about 1100 MeV/G (e.g., Fig. D5), AP-8 protons vanish in the neighborhood of L = 5 R_E; for μ values larger than this (e.g., Fig. D6), the region devoid of trapped protons expands both inward and outward. Additional

examples of this effect will be given in Subsection E, L-dependence. For magnetic moments larger than about 2700 MeV/G, the AP-8 phase-space density vanishes on all L-shells specified by Eq. (1).

(3) As a function of K, the *form* of the proton phase-space density varies systematically with μ and L-shell; no characteristic function, simply multiplied by different amplitudes, is apparent.

(4) For large magnetic moments, the K-dependence of the phase-space density is exponential, with maxima at the magnetic equator (K = 0) and vanishing beyond a cutoff value, K_c; these cutoff values vary with μ and L.

(5) The cutoff values vary systematically with magnetic moment and L-shell and are smaller than those estimated for the atmospheric loss cone. The proton penetration depth into the atmosphere very likely differs from that of electrons; thus, the assumption of loss at the same 100-km altitude used for the electrons to estimate the size of loss cone should be (but has not yet been) reconsidered for protons.

The cutoff values of the geometrical invariant K are plotted as functions of magnetic moment μ for the nine L-shells (indicated by the labels) specified in Figs. 3 and 4.

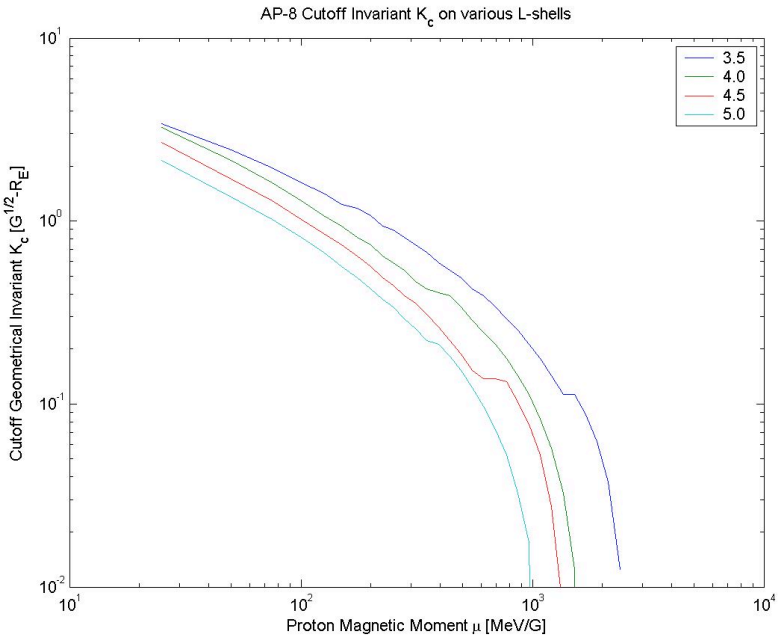

Figure 3. Cutoff invariant K_c as functions of μ for the four inner L-shells. AP-8 phase-space density vanishes in the regions above and to the right of the curves. The trapping region decreases systematically on L-shells larger than 3.5 R_E.

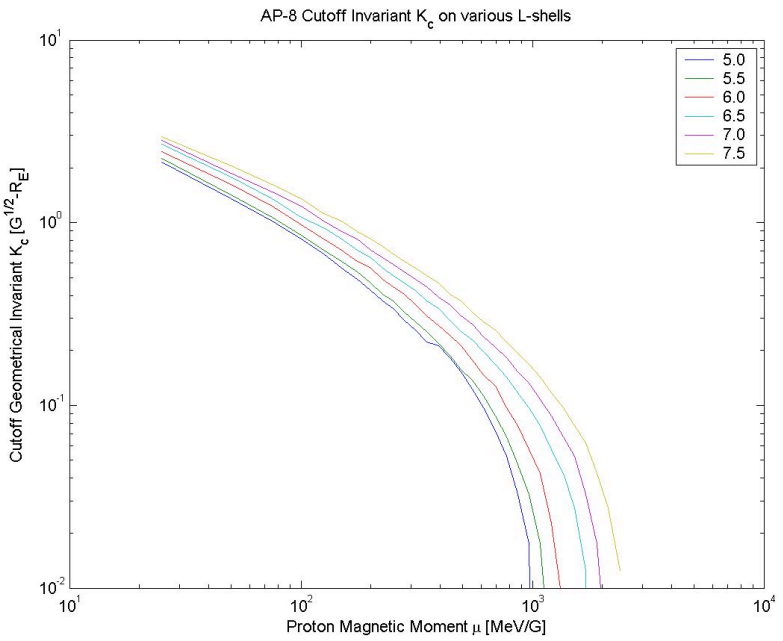

Figure 4. Cutoff invariant K_c as functions of μ for the six outer L-shells. AP-8 phase-space density vanishes in the regions above and to the right of the curves. The trapping region increases systematically on L-shells larger than 5.0 R_E. (7.5 R_E is an extrapolation.)

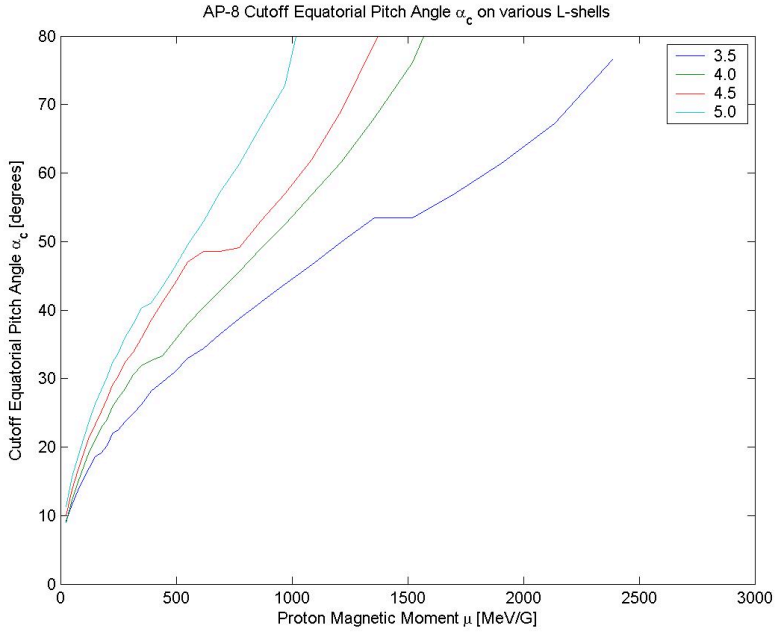

Figure 5. Cutoff equatorial pitch angle α_c as functions of μ on four inner L-shells. AP-8 phase-space density vanishes in the regions below and to the right of the curves. The trapping region decreases systematically on L-shells larger than 3.5 R_E.

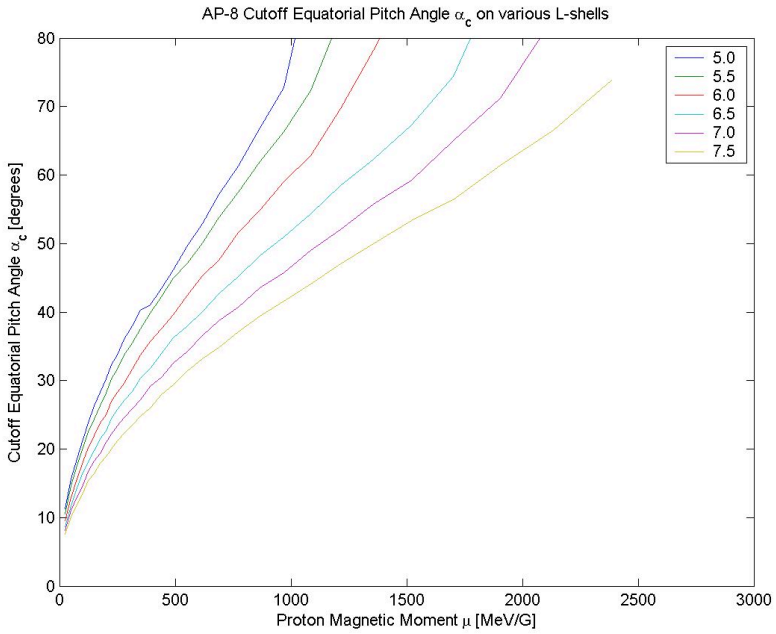

Figure 6. Cutoff equatorial pitch angle α_c as functions of μ on 6 outer L-shells. AP-8 phase-space density vanishes in the regions below and to the right of the curves. The trapping region increases systematically on L-shells larger than 5.0 R_E. (7.5 R_E is an extrapolation.)

The cutoff values, K_c, correspond directly to cutoff values of the equatorial pitch angle, α_c, below which the phase-space density vanishes; these cutoff values of the equatorial pitch angle α are plotted as functions of magnetic moment μ in Figs. 5 and 6 for the nine L-shells specified. These four figures suggest that momentum-dependent trapping boundaries, perhaps drift-type loss cones (i.e., open drift shells), serve as boundary conditions for the trapped proton population represented in the AP-8 model environment.

E. L-dependence

The first feature of the AP-8 proton phase-space density, described in Subsection D, K-dependence, was that local minima occur near L = 5 R_E. To illustrate this, a subset of the results in Figs. D1–D6, was sorted into L profiles, with the invariants μ and K held fixed; a number of intermediate L-shell values were also added to improve the resolution of the profiles. Figure 7 shows four phase-space density profiles for a fixed value of μ = 150.0 MeV/G and four fixed values of K, 0.0, 0.2, 0.4, and 0.6 $G^{1/2}$-R_E.

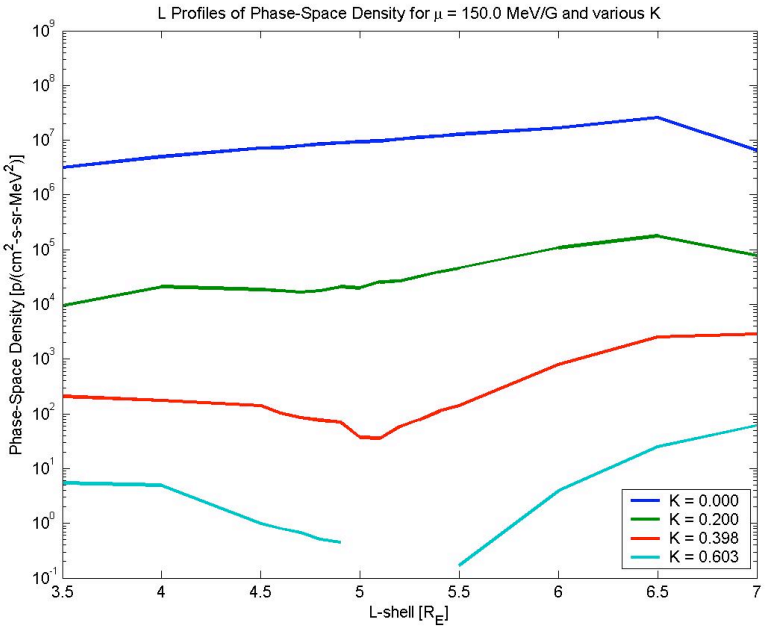

Figure 7. L-dependence of AP-8 phase-space density for fixed μ and K. When K = 0.603, the phase-space density vanishes on L-shells between 5.0 and 5.4 R_E.

On the magnetic equator, K = 0, the AP-8 phase-space density for μ = 150 MeV/G increases monotonically with L between 3.5 R_E and 6.5 R_E but then decreases beyond 6.5 R_E. For K values larger than 0.3631 and L values between 6.5 R_E and 7.0 R_E, the phase-space density rolls off but does not decrease with increasing L. Local minima develop in the central region; this implies a pitch-angle distribution more strongly peaked in the neighborhood of L = 5 R_E than near either end, 3.5 R_E or 7.0 R_E. For μ = 150 MeV/G and K > 0.5495 $G^{1/2}$-R_E, the AP-8 phase-space density vanishes at L = 5.0 R_E; as the K value increases, the region devoid of protons expands both outward and inward: for K > 0.8712 $G^{1/2}$-R_E, the phase-space density vanishes in the whole outer region. For K > 1.202 $G^{1/2}$-R_E, the phase-space density vanishes throughout the valid region for the AP-8 model considered here, 3.5 R_E < L < 7.0 R_E.

Figure 8 shows four phase-space density profiles for a fixed value of μ = 313.29 MeV/G and another four fixed values of K, 0.0, 0.1, 0.2, and 0.302 $G^{1/2}$-R_E.

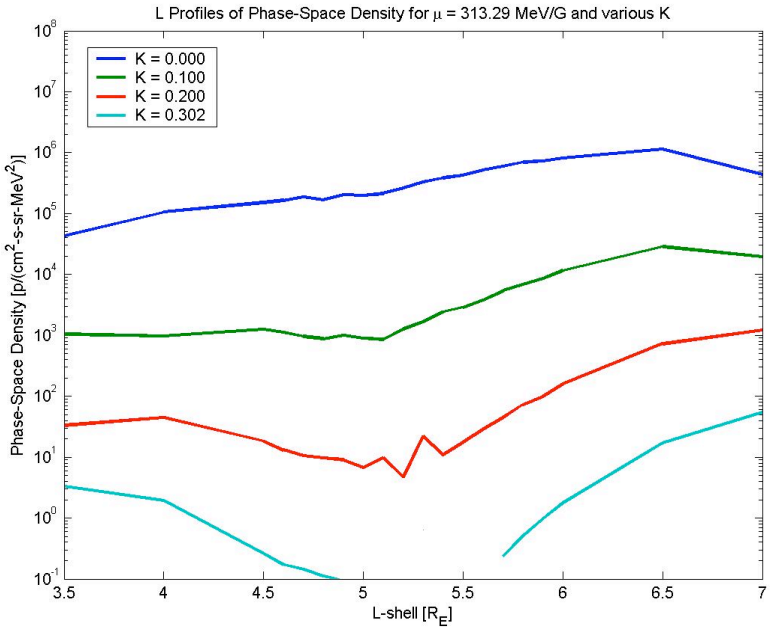

Figure 8. L-dependence of AP-8 phase-space density for fixed μ and K. When K = 0.302, the phase-space density vanishes on L-shells between 5.0 and 5.6 R_E.

The profiles for the two smaller K values (< 0.140) decrease between 6.5 R_E and 7.0 R_E, while the profiles for the two larger K values (> 0.140) roll off but do not decrease, as in Fig. 7. Local minima develop in the central region. For μ = 313.29 MeV/G and K > 0.2550 $G^{1/2}$-R_E, the AP-8 phase-space density vanishes at L = 5.0 R_E; as the K value increases, the region devoid of protons expands both outward and inward. For K > 0.4786 $G^{1/2}$-R_E, the phase-space density vanishes in the whole outer region. For K > 0.7244 $G^{1/2}$-R_E, the phase-space density vanishes throughout the valid region for the AP-8 model considered here, 3.5 R_E < L < 7.0 R_E.

Figure 9 shows four phase-space density profiles for a fixed value of μ = 491.97 MeV/G and another four fixed values of K, 0.000, 0.050, 0.100, and 0.150 $G^{1/2}$-R_E.

As in Figs. 7 and 8, the profiles for the two smaller K values (< 0.055) decrease, those for the two larger K values (> 0.055) roll off between 6.5 R_E and 7.0 R_E, and local minima develop in the central region. For μ = 491.97 MeV/G and K > 0.155 $G^{1/2}$-R_E, the AP-8 phase-space density vanishes at L = 5.0 R_E; as the K value increases, the region devoid of protons expands both outward and inward. For K > 0.3020 $G^{1/2}$-R_E, the phase-space density vanishes in the whole outer region. For K > 0.4786 $G^{1/2}$-R_E, the phase-space density vanishes throughout the valid region for the AP-8 model, 3.5 R_E < L < 7.0 R_E, considered here.

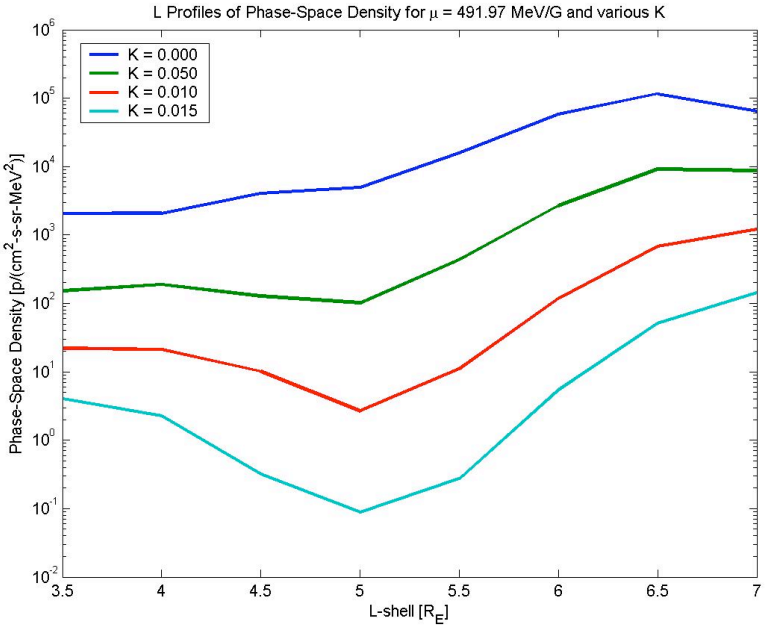

Figure 9. L-dependence of AP-8 phase-space density for fixed μ and K.

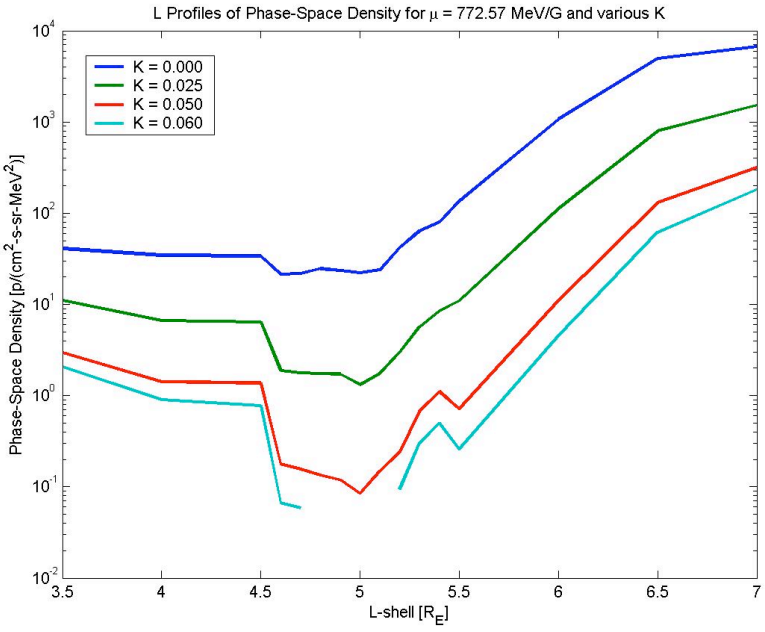

Figure 10. L-dependence of AP-8 phase-space density for fixed μ and K. When K = 0.060, the phase-space density vanishes on L-shells between 4.8 and 5.1 R_E.

Figure 10 shows four profiles for a fixed value of μ = 772.57 MeV/G and another four fixed values of K, 0.000, 0.025, 0.050, and 0.060 $G^{1/2}$-R_E.

For μ = 772.57 MeV/G, all four profiles exhibit local minima, and all roll off but do not decrease between 6.5 R_E and 7.0 R_E. In this case, the AP-8 phase-space density vanishes at L = 5.0 R_E for K > 0.050 $G^{1/2}$-R_E; as the K value increases, the region devoid of protons expands both outward and inward. For K > 0.180 $G^{1/2}$-R_E, the phase-space density vanishes in the whole outer region. For K > 0.290 $G^{1/2}$-R_E, the phase-space density vanishes throughout the valid region for the AP-8 model considered here, 3.5 R_E < L < 7.0 R_E.

Figure 11 shows four profiles for a fixed value of μ = 1083.8 MeV/G and another five fixed values of K, 0.000, 0.005, 0.010, 0.015, and 0.020 $G^{1/2}$-R_E. As in Fig. 10, all four profiles exhibit local minima, and all roll off but do not actually decrease between 6.5 R_E and 7.0 R_E.

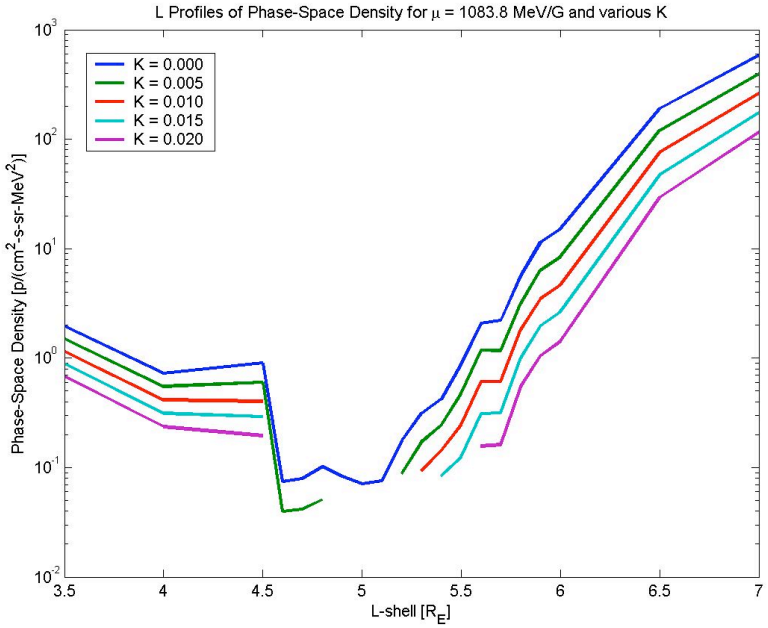

Figure 11. L-dependence of AP-8 phase-space density for fixed μ and K. When K = 0.005, the phase-space density vanishes on L-shells from 4.9 to 5.1 R_E; when K = 0.010, from 4.6 to 5.2 R_E; when K = 0.015, from 4.6 to 5.3 R_E; when K = 0.020, from 4.6 to 5.5 R_E.

In Fig. 11, the AP-8 phase-space density vanishes at L = 5.0 R_E for K > 0.001 $G^{1/2}$-R_E; as the K value increases, the region devoid of protons expands both outward and inward. For K > 0.105 $G^{1/2}$-R_E, the phase-space density vanishes in the whole outer region. For K > 0.175 $G^{1/2}$-R_E, the phase-space density vanishes throughout the valid region for the AP-8 model considered here, 3.5 R_E < L < 7.0 R_E.

5. Discussion

In the parameter space (μ, K, L), the phase-space densities of both electrons from AE-8 and protons from AP-8 exhibit three characteristic gradients. In each case, the phase-space density *decreases* with increasing μ and *decreases* with increasing K (with maxima at K = 0). The electron phase-space density *increases* with increasing L, with larger gradients in the inner region, 3.5 R_E < L < 5.5 R_E, and much weaker gradients in the outer region, 5.5 R_E < L < 7.5 R_E. The proton phase-space density, on the other hand, *increases* with increasing L in region 5.0 < L < 6.5 R_E but in most cases *decreases* with increasing L in the region 3.5 R_E < L < 5.0 R_E. The proton phase-space density exhibits local minima near L = 5.0 R_E. Along GPS-type orbits, L and K change simultaneously, and one consequence of the oppositely directed gradients is that differently shaped counting rate profiles may occur in the same local time zone during geomagnetically quiet intervals. The actual profile will depend in detail on the actual gradients encountered along the orbit (these constitute additional degrees of freedom). Figure 12 shows the counting rates recorded in the P1 Channel of the BDD-IIR instrument on GPS Navstar 41 for six passes through the magnetic equator (12 hours apart) during 15–17 December 2000. These data fall into two distinct sets, shown by red and blue lines, with the passes for each color taking place 24 hours apart.

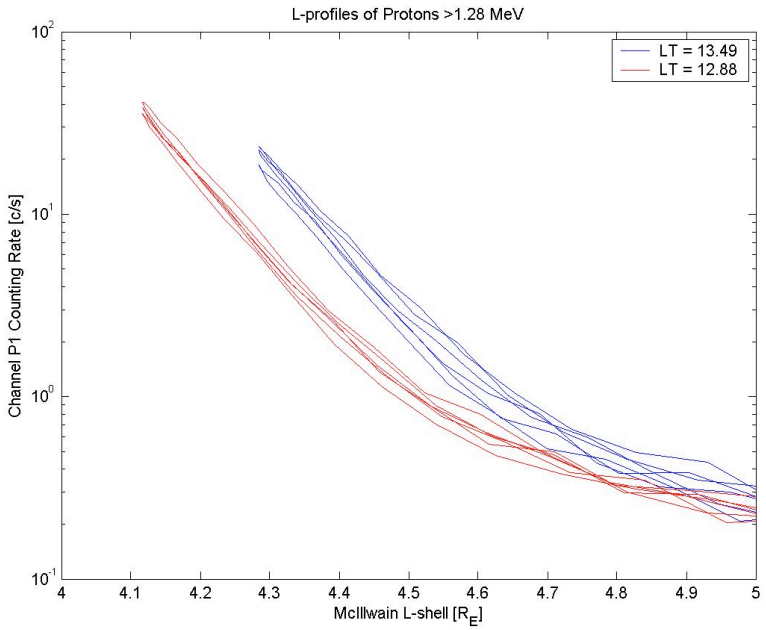

Figure 12. BDD-IIR channel P1 counting rates recorded during 15–17 December 2000.

The local times for the magnetic equator crossings are shown in the box and differ by only 0.61 h. The persistence of the different profiles rules out temporal changes as a dominant effect. Features similar to these, albeit less pronounced, also appear regularly in high-energy electron channels of GPS instruments. As Schulz has observed,[16] profiles of counting rates above a fixed energy threshold like those plotted in Fig. 12 provide a less than optimal picture of the underlying radial-transport processes and their consequences.

The proton data extracted from channels P1 (shown in Fig. 12) and E1 were analyzed as follows: The counting rates for the two channels were modeled as sums of two contributions—nonproton "background" counts, plus counts due to a spectrum of incident protons. Background counts in channel P1, arising from cosmic rays and >1.2 MeV electrons, are approximately the same as the counts recorded in channel P2; the difference, P1 – P2, corresponds to a proton in the energy range 1.28–5.3 MeV. The background for channel E1, arising from cosmic rays and electrons >0.1 MeV, was estimated from model counts obtained by evaluating integrals of the E1 response function, with electron spectra inferred from the other electron channels. An exponential energy spectrum was assumed for the incident protons, and its parameters were determined from the two rather broad channels, 0.34–1.28 MeV (E1) and 1.28–5.3 MeV (P1 – P2). Dividing the differential proton flux by $p^2/2m_0$ yields the proton phase-space density, which may be evaluated as a function of transverse invariant μ for each accumulation, using an appropriate model magnetic field. (Note that the procedure used for the wide-field-of-view BDD-IIR data is exactly the same as used above with the AE-8 and AP-8 omnidirectional model fluxes.) For the same data shown in Fig. 12, results of the phase-space density analysis are plotted (along with empirically fitted curves) in Figs. 13–15 for fixed μ values 199.05, 315.48, and 500.00 MeV/G.

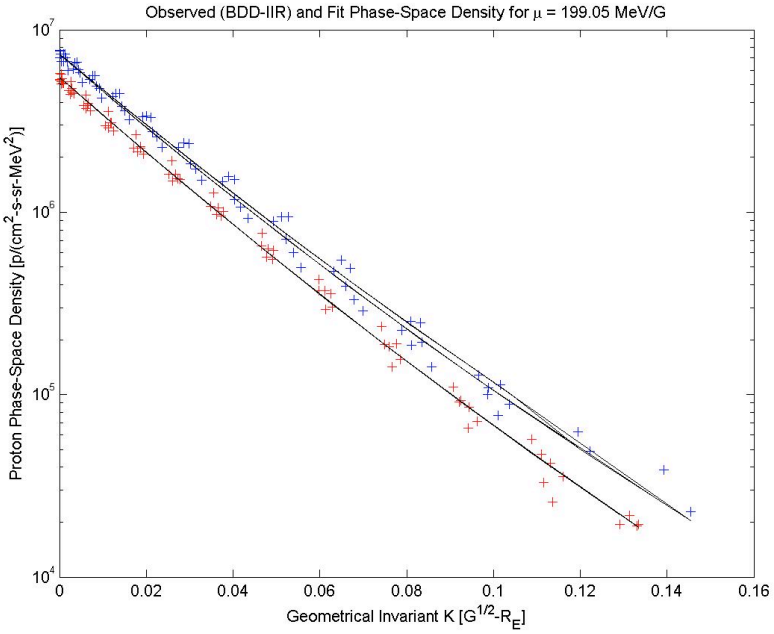

Figure 13. BDD-IIR phase-space density at constant μ = 199.05 MeV/G.

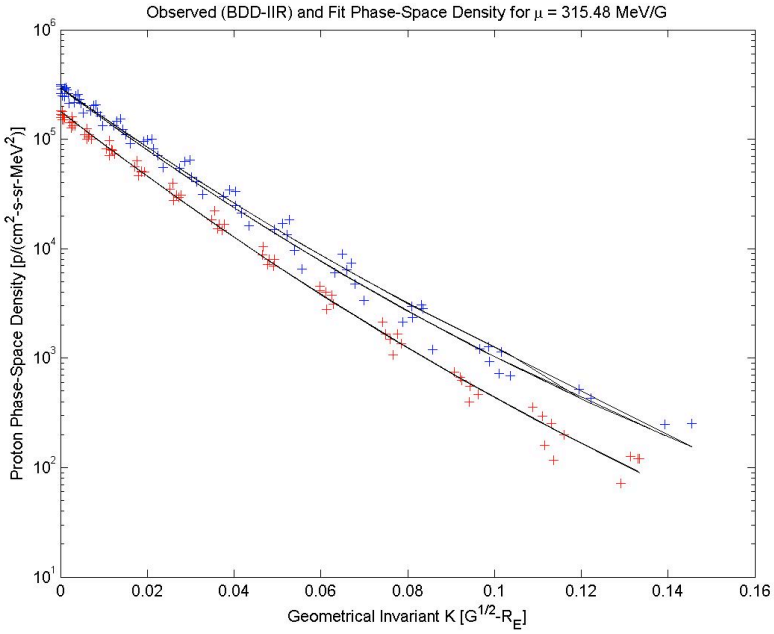

Figure 14. BDD-IIR phase-space density at constant μ = 315.48 MeV/G.

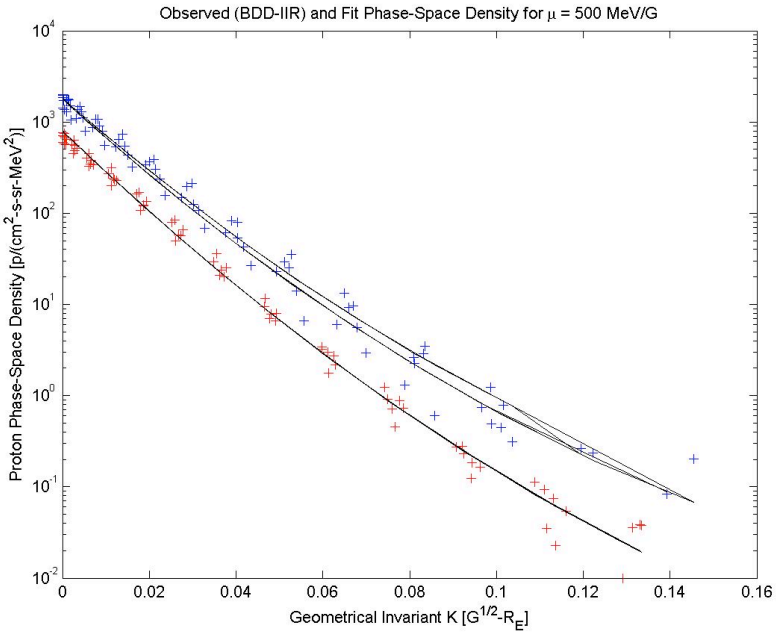

Figure 15. BDD-IIR phase-space density at constant μ = 500.00 MeV/G.

The lines plotted in Figs. 13–15 are least-squares fits to the points of a 4-parameter representation of the phase-space density suggested by features observed in the AP-8 model

(Figs. D1b–D3b)—namely, a decreasing exponential dependence upon K, with scale lengths that increase with increasing L and an increasing exponential dependence upon L:

$$\log(f) = A - B\,K + C\,L + D\,(L \times K), \tag{13}$$

where A, B, C, and D are the parameters; and L and K, the geomagnetic coordinates evaluated from the Tsyganenko 1989 model magnetic field. For the cases shown, the best-fit values of the four parameters are shown in Table 1.

Table 1. Best-fit parameters for Eq. 13

μ	A	B	C	D
199.05	8.3716	95.9325	1.7366	9.6808
315.48	0.0092	177.692	2.9372	22.858
500.00	-13.244	307.262	4.8401	43.740

The characteristics of the proton phase-space density observed by BDD-IIR are thus similar to those of the AP-8 model environment—a positive gradient with respect to L that becomes stronger for larger μ values, a strong negative gradient with respect to K, and a scale length that decreases with increasing μ but increases with increasing L. This variation of the scale length is consistent with the L and μ dependence on the cutoff invariant K_c given in Fig. 4, where K_c increases with increasing values of L but decreases with increasing values of μ. For simple exponential functions of K, the characteristic scale length, of course, corresponds to the critical value K_c (two equivalent specifications of the same line).

Returning now to the model environments, one of the most striking features of the AP-8 and AE-8 models is the momentum-dependent cutoff value of the equatorial pitch angle, α_c, below which the phase-space density (or the corresponding geometrical invariant, K_c) vanishes. It was found empirically that, for the L-shell range $5.0\ R_E < L < 7.5\ R_E$, the cutoffs for both electrons and protons are represented reasonably well by a scaling law,

$$\sin(\alpha_c) = 0.064205\ m_0^{0.2018}\ \mu^{0.4677}\ L^{-1.1131}, \tag{14}$$

where the electron rest mass and transverse invariant values are used for the electron cutoffs; and proton rest mass and transverse invariant values, for proton cutoffs. What physical process, if any, might be responsible for cutoffs characterized by this scaling is unknown. The energy spectra of the AE-8 and AP-8 models themselves involve maximum energies beyond which the flux vanishes, and this clearly is the same feature under consideration here: as μ increases, the returned flux corresponds to higher and higher energy until the maximum energy is exceeded and the flux vanishes. Indeed, both the AE-8 model and the AP-8 model set a minimum value of 1 particle/cm^2-s for the integral flux;[1] therefore, the critical values

correspond to a threshold value of the integral flux—a practical limit rather than absolute one (by comparison, the cosmic-ray flux is about 2 particles/cm^2-s). In any event, the maximum (cutoff) energy varies systematically, decreasing with increasing B/B_0 and decreasing with increasing L. An important issue for future work is to validate these limits with measurements which have become available since the models were completed and then to understand the physical processes responsible for such trapping boundaries if they are present in earth's magnetosphere.

6. Conclusion

The AE-8 trapped electron and the AP-8 trapped proton model environments provide global estimates of omnidirectional integral fluxes of energetic particles trapped in the earth's geomagnetic field for a given particle energy and position in the magnetosphere, parameterized in terms of L-shell and the magnetic-field-line ratio, B/B_0. These empirical models incorporate experimental results from many different instruments and investigators and represent the latest generation of a family of such empirical models with a legacy of nearly four decades. The model returns flux above a set of threshold energies, similar in spirit to the output of energetic particle instruments. Estimates of the differential particle fluxes are obtained by differencing the integral fluxes from adjacent energies. These empirical models provide a reasonable picture of the global spatial distribution of the trapped particle population, even though their primary application has been for engineering studies, such as dose estimation, radiation damage, and shielding requirements.

These models were used here to examine the L-shell variation of phase-space densities for sets of transverse invariants, μ, and geometrical invariants, K; variation due to particle rest mass was considered as well. Both models were characterized by three gradients in the parameter space (μ, K, L): the phase-space density *decreases* with increasing μ; *decreases* with increasing K; and, for the most part, *increases* with increasing L. More specifically, the electron phase-space density *increases* with increasing L, with larger gradients in the inner region, $3.5\ R_E < L < 5.5\ R_E$, and much weaker gradients in the outer region, $5.5\ R_E < L < 6.5\ R_E$. The proton phase-space density, on the other hand, exhibits local minima near $L = 5.0\ R_E$: it *increases* with increasing L in region $5.0 < L < 6.5\ R_E$ but in most cases *decreases* with increasing L in the region $3.5\ R_E < L < 5.0\ R_E$.

The general functional dependence of phase-space density upon the invariants, a dependence suggested by the AE-8 and the AP-8 models, was applied in the analysis of some GPS proton data. Inclusion of oppositely directed K- and L-gradients of the phase-space density for fixed values of the transverse invariant yielded a description closer to optimal than did simple profiles of flux (or counting rate) above a fixed threshold energy. Along GPS orbits, the parameters L and K vary simultaneously. The characteristics of the proton phase-space density observed by BDD-IIR are therefore similar to those of the AP-8 model environment: a positive gradient with respect to L that becomes stronger for larger μ values, a strong negative gradient with respect to K, and a scale length that decreases with increasing μ but increases with increasing L.

The presence of local minima near $L = 5\ R_E$ exhibited by the AP-8 proton phase-space density suggests that significant loss processes dominate high-momentum protons in this

region of the magnetosphere, roughly 4.5 R_E < L < 5.5R_E. Further research should be undertaken to validate this feature and to identify the physical processes responsible for this apparent loss of the high-momentum protons.

Both the AE-8 and the AP-8 models exhibit critical or cutoff values of the invariants beyond which the phase-space density vanishes. For both electrons and protons, these cutoff values vary systematically with transverse invariant and L-shell and are smaller than those estimated for the atmospheric loss cone. For large transverse invariants, for both electrons and protons, the K-dependence of the phase-space density is exponential, with maxima at the magnetic equator and vanishing beyond the cutoff value K_c. The equatorial pitch angles corresponding to these cutoff geometrical invariants appear to be related to the *rest mass*, the *transverse invariant*, and the *L-shell* by an empirical scaling law. Such features suggest that momentum-dependent trapping boundaries, perhaps drift-type loss cones, may serve as boundary conditions for the trapped populations of electrons and protons.

Acknowledgments

The author benefited from helpful discussions with and comments by Reiner Friedel, Peter Gary, Chuck Ingraham, Michelle Thomsen, Michel Tuszewski, and Sorin Zaharia. All work reported herein was performed under the auspices of the United States Department of Energy.

References

1. J. I. Vette, “The AE-8 Trapped Electron Model Environment,” Goddard Space Flight Center report NSSDC/WDC-A-R&S 91-24 (1991).
2. D. M. Sawyer and J. I. Vette, “AP-8 Trapped Proton Environment for Solar Maximum and Solar Minimum,” Goddard Space Flight Center report NSSDC/WDC-A-R&S 76-06 (1976).
3. J. I. Vette, “Inner Zone Protons and Electrons,” *Models of the Trapped Radiation Environment,* Vol. I, NASA SP-3024 (1966).
4. J. I. Vette, A. B. Lucero, and J. A. Wright, “Electrons at Synchronous Altitudes,” *Models of the Trapped Radiation Environment,* Vol. II, NASA SP-3024 (1966).
5. J. I. Vette and A. B. Lucero, “Inner and Outer Zone Electrons,” *Models of the Trapped Radiation Environment,* Vol. III, NASA SP-3024 (1967).
6. G. W. Singley and J. I. Vette, “The AE-4 Model of the Outer Radiation Zone Electron Environment,” Goddard Space Flight Center report NSSDC 72-06 (1972).
7. G. W. Singley and J. I. Vette, “A Model Environment for Outer Zone Electrons,” Goddard Space Flight Center report NSSDC 72-13 (1972).
8. J. H. King, “Low Energy Protons,” *Models of the Trapped Radiation Environment,* Vol. IV, NASA SP-3024 (1967).

9. J. P. Lavine and J. I. Vette, "Inner Belt Protons," *Models of the Trapped Radiation Environment,* Vol. V, NASA SP-3024 (1969).

10. T. E. Cayton, R. D. Belian, S. P. Gary, T. A. Fritz, and D. N. Baker, "Energetic Electron Components at Geosynchronous Orbit," *Geophys. Res. Lett.* **16**, 147 (1989).

11. A. Vampola, "Outer Zone Energetic Electron Environment Update," ESA Final Report (2002).

12. T. W. Armstrong and B. L. Colborn, "Evaluation of Trapped Radiation Model Uncertainties for Spacecraft Design," NASA Report NASZ/CR-2000-210072 (2000).

13. W. D. Pesnell, "Fluxes of Relativistic Electrons in Low-Earth Orbit during the Decline of Solar Cycle 22," *IEEE Trans. Nucl. Sci.* **48**, 2016 (2001).

14. T. E. Cayton and D. M. Pongratz, "Dosimetry Results from the Global Positioning System Satellite Navstar 10, Mission Summary," Los Alamos National Laboratory reports LA-UR-05-1183 (2005) and LA-14232 (2005).

15. A. J. Chen and D. P. Stern, "Adiabatic Hamiltonian of Charged Particle Motion in a Dipole Field," *J. Geophys. Res.* **80**, 690 (1975).

16. M. Schulz, "The Magnetosphere," in *Geomagnetism,* Vol. 4, ed. by J. A. Jacobs, Academic Press, San Diego, 1991, p. 171.

17. D. M.. Palmer, S. Barthelmy, N. Gehrels, R. M. Kippen, T. Cayton, C. Kouveliotou, D. Eichler, R. A. M. J. Wijers, P. M. Woods, J. Granot, Y. E. Lyubarsky, E. Ramirez-Ruiz, L, Barbier, M. Chester, J. Cummings, E. E. Fenimore, M. H. Finger, B. M, Gaensler, D. Hullinger, H. Krimm, C. B. Markwardt, J. A. Nousek, A. Parsons, S. Patel, T. Sakamoto, G. Sato, M. Suzuki, and J. Tueller, "A Giant γ-ray Flare from the Magnetar SGR 1806-20," *Nature* **434**, 1107 (2005).

18. T. E. Cayton, "An Investigation of the Performance of the CXD HXP1 Particle Channel Electronics and Logics Using Random Pulser Stimulation," Los Alamos National Laboratory report LA-UR-05-4760.

19. S. P. Christon, D. G. Mitchell, D. J. Williams, L. A. Frank, C. Y. Huang, and T. E. Eastman, "Energy Spectra of Plasma Sheet Ions and Electrons from ~50 eV/e to ~1 MeV during Plasma Temperature Transitions," *J. Geophys. Res.* **93**, 2562 (1988).

Appendix A: AE-8 Phase-Space Density as Functions of μ

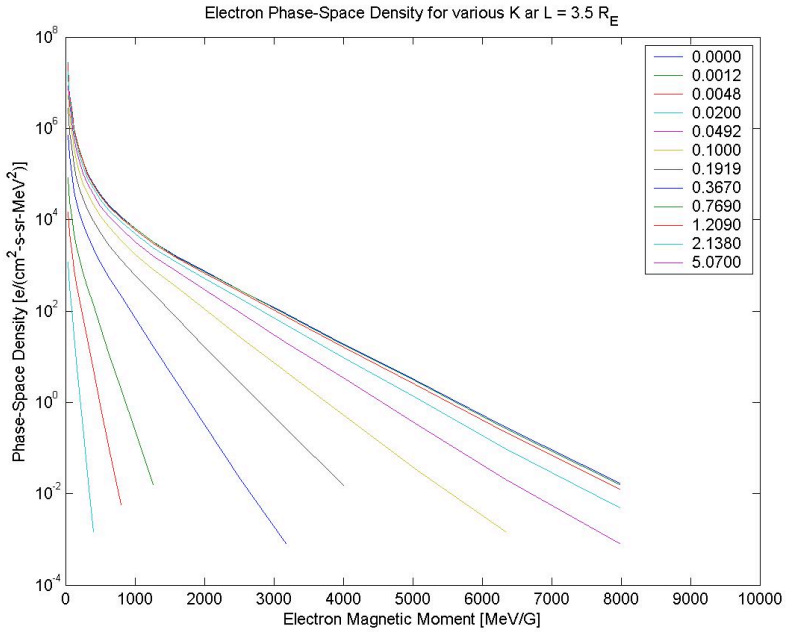

Figure A1. AE-8 phase-space density at L = 3.5 as functions of μ for twelve values of K.

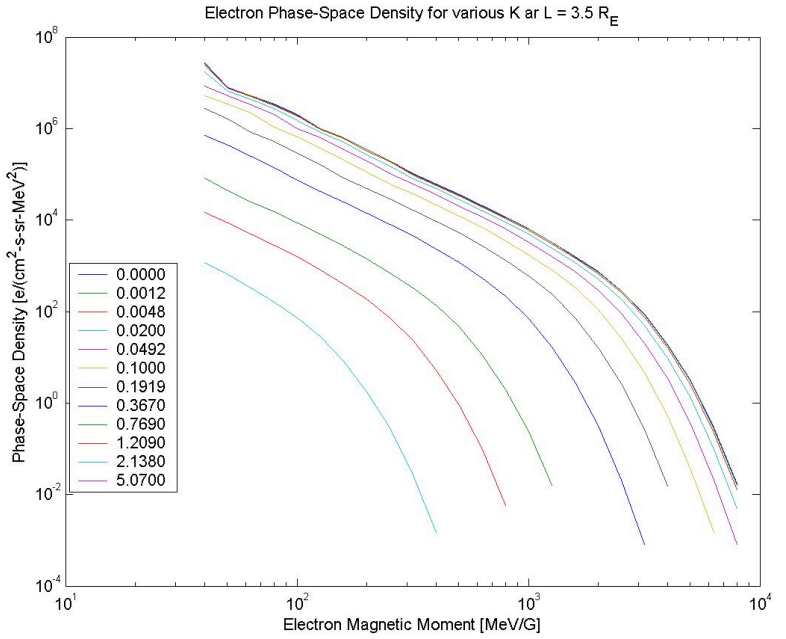

Figure A2. The same quantities as in Fig. A1 but in log-log format.

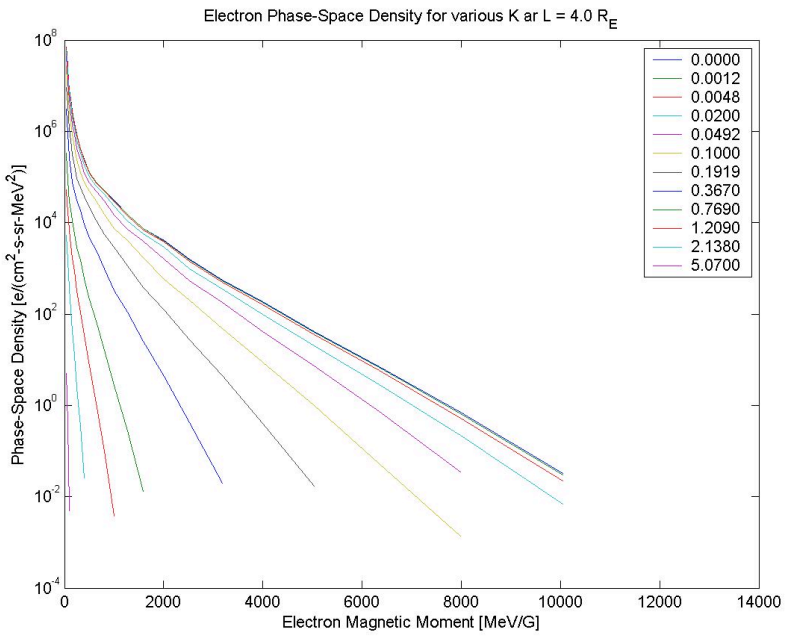

Figure A3. AE-8 phase-space density at L = 4.0 as functions of μ for twelve values of K.

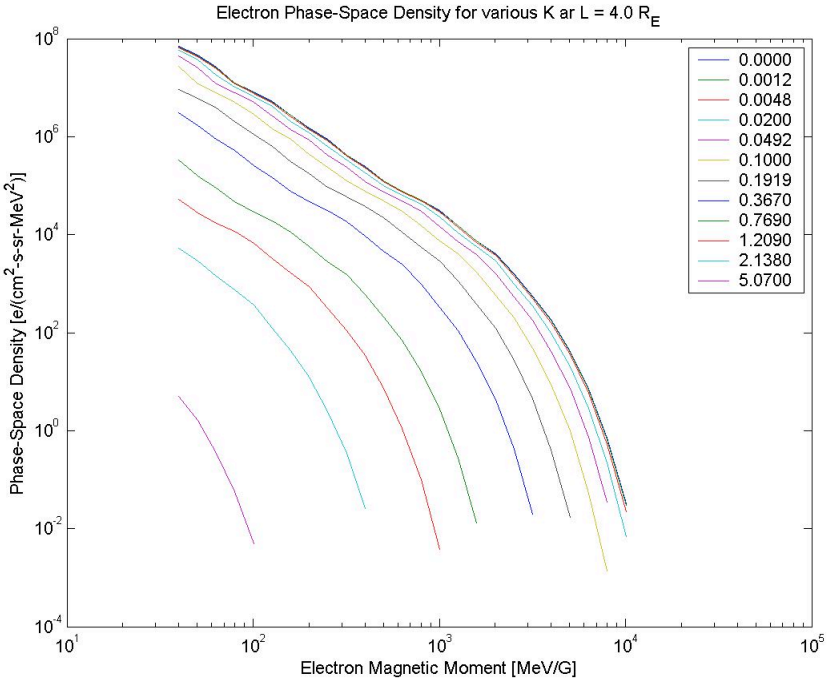

Figure A4. The same quantities as in Fig. A3 but in log-log format.

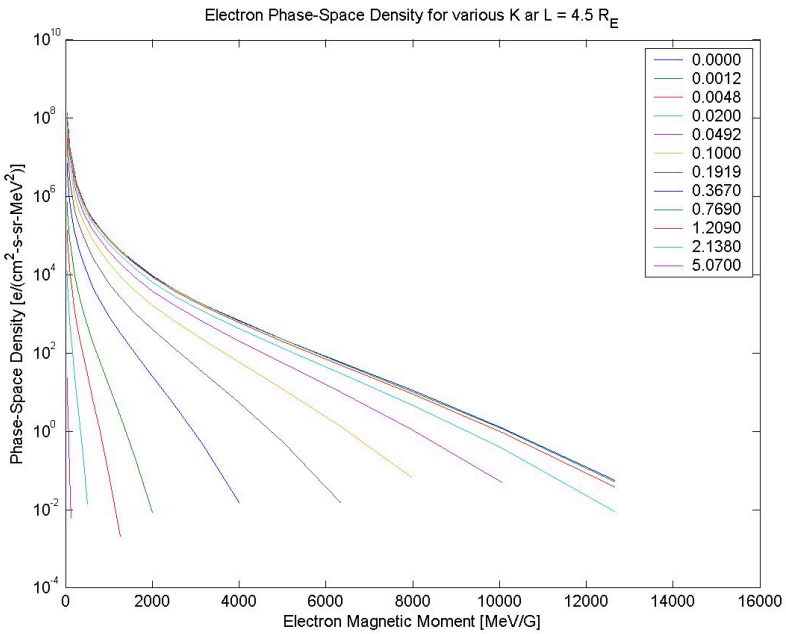

Figure A5. AE-8 phase-space density at L = 4.5 as functions of μ for twelve values of K.

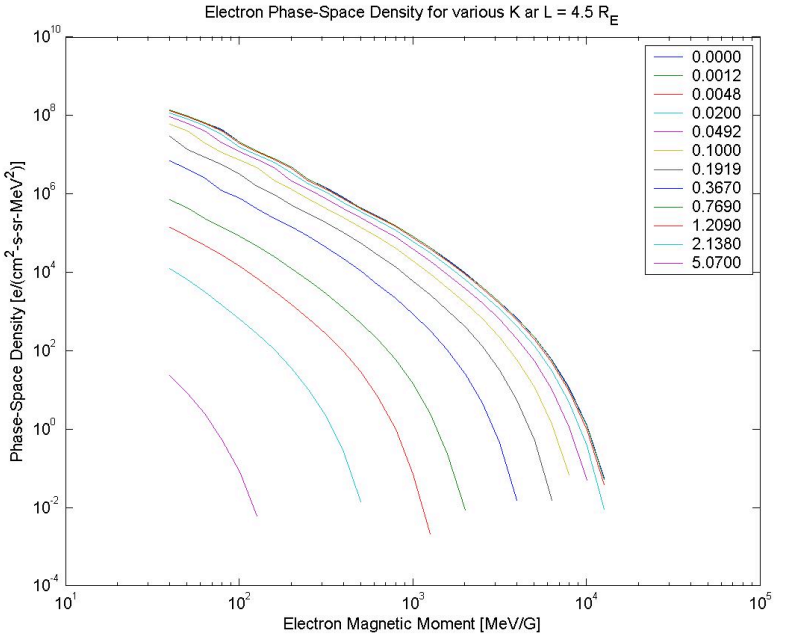

Figure A6. The same quantities as in Fig. A5 but in log-log format.

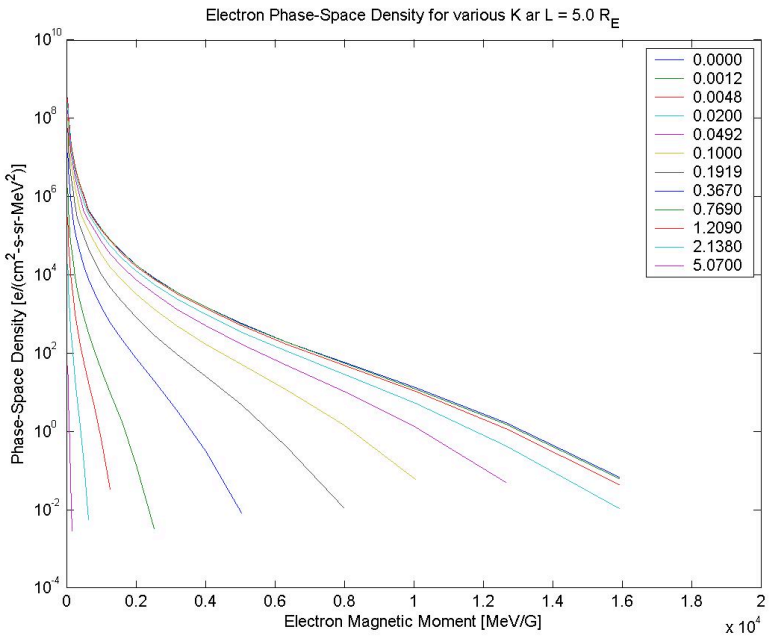

Figure A7. AE-8 phase-space density at L = 5.0 as functions of μ for twelve values of K.

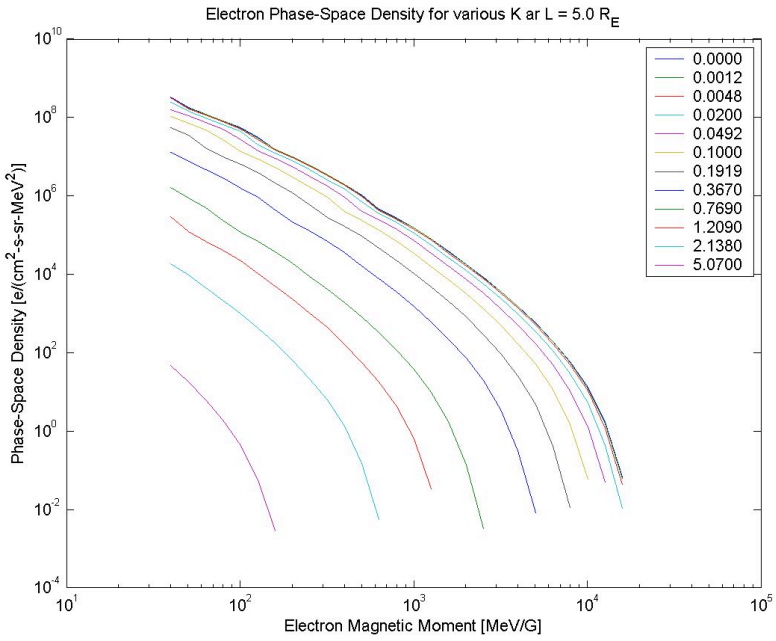

Figure A8. The same quantities as in Fig. A7 but in log-log format.

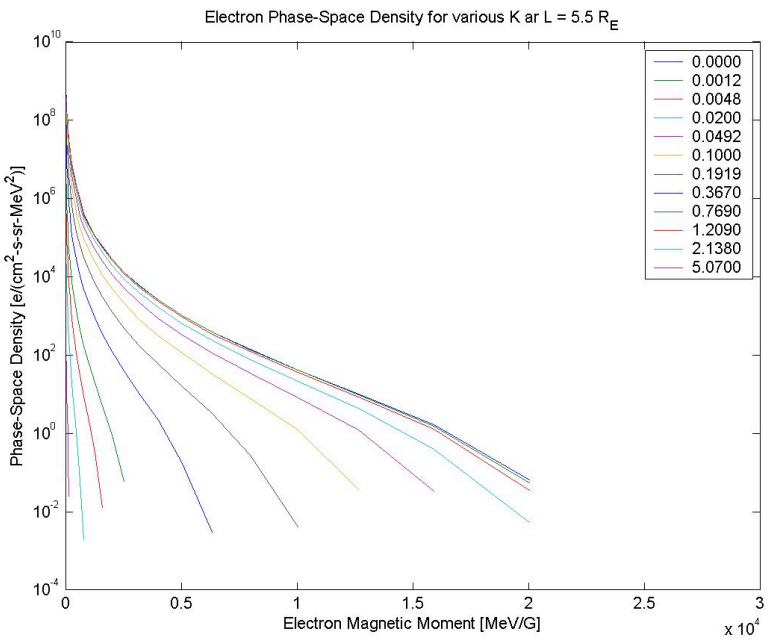

Figure A9. AE-8 phase-space density at L = 5.5 as functions of μ for twelve values of K.

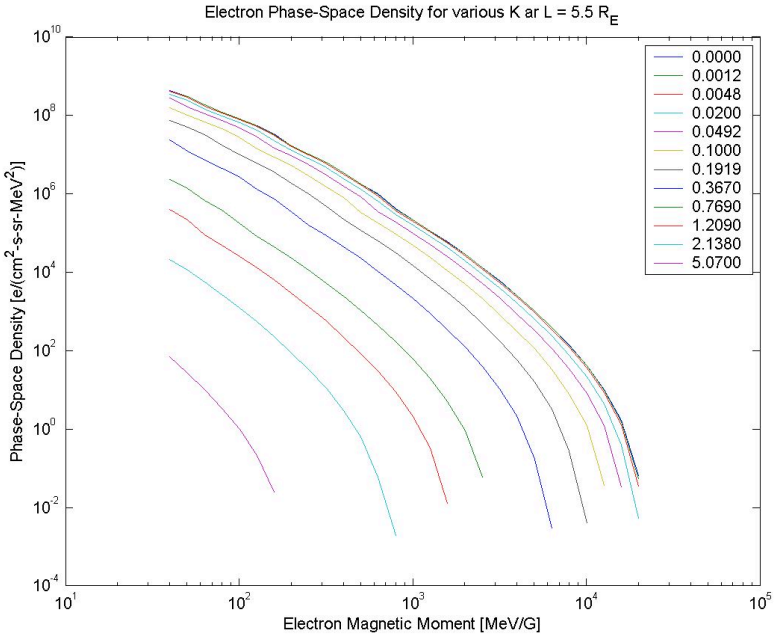

Figure A10. The same quantities as in Fig. A9 but in log-log format.

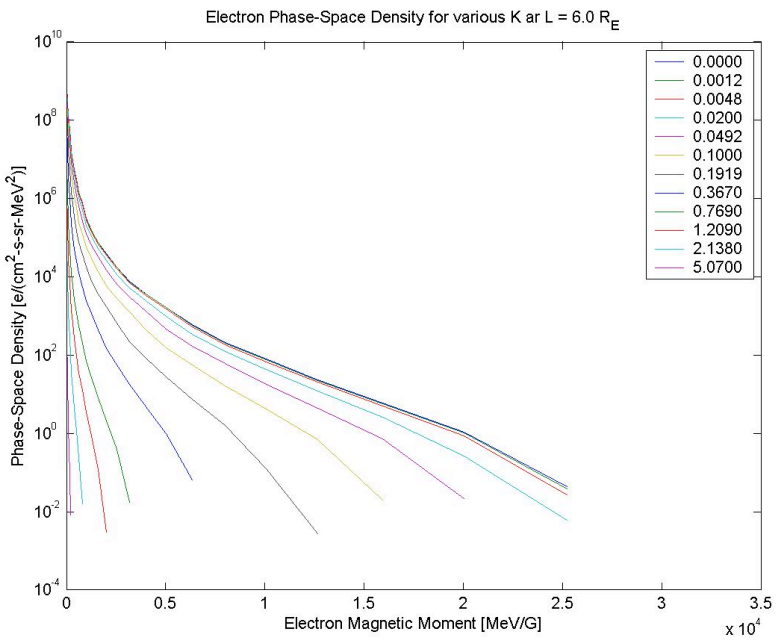

Figure A11. AE-8 phase-space density at L = 6.0 as functions of μ for twelve values of K.

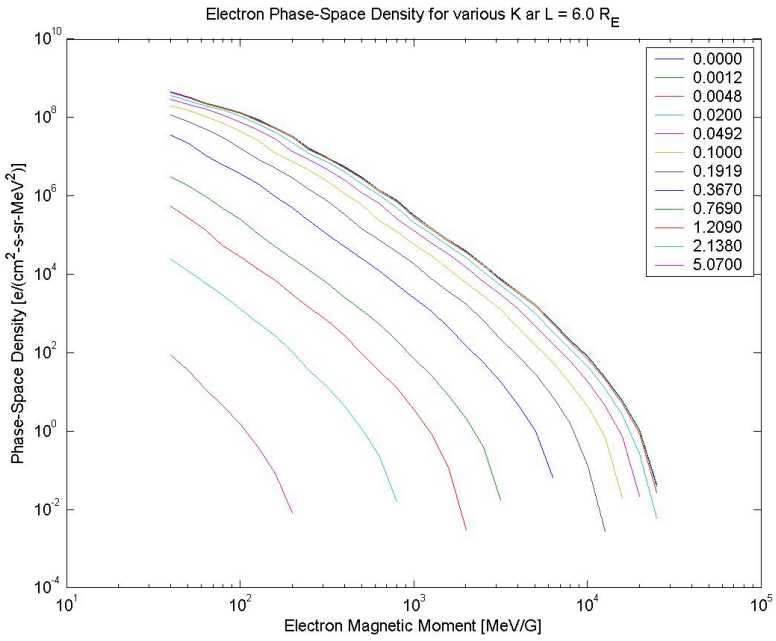

Figure A12. The same quantities as in Fig. A11 but in log-log format.

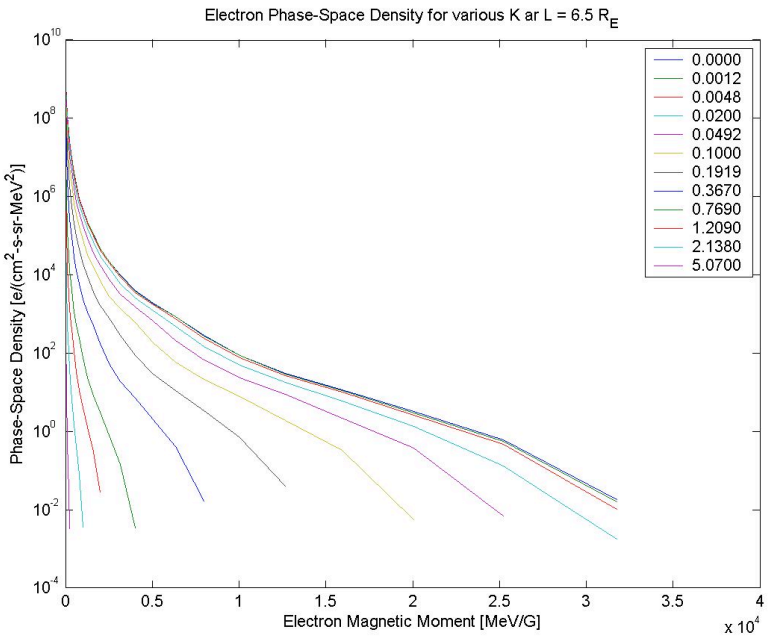

Figure A13. AE-8 phase-space density at L = 6.5 as functions of μ for twelve values of K.

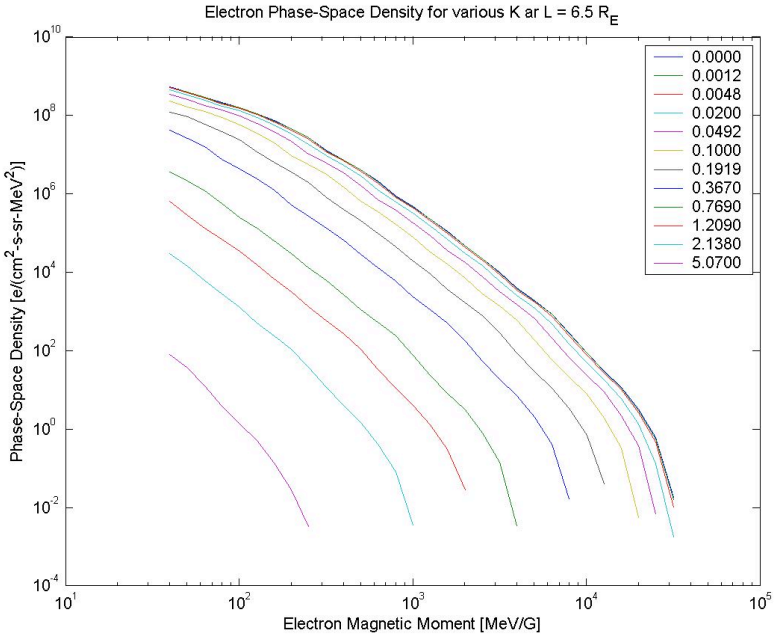

Figure A14. The same quantities as in Fig. A13 but in log-log format.

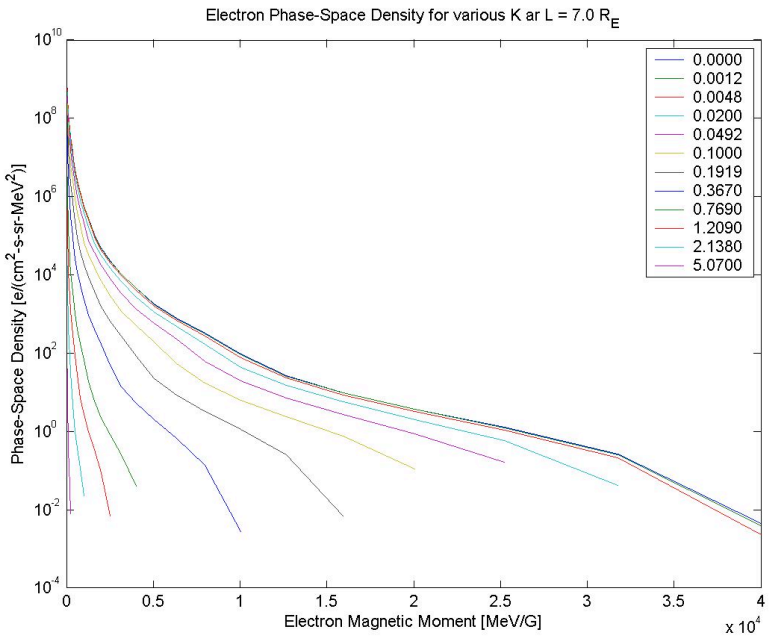

Figure A15. AE-8 phase-space density at L = 7.0 as functions of μ for twelve values of K.

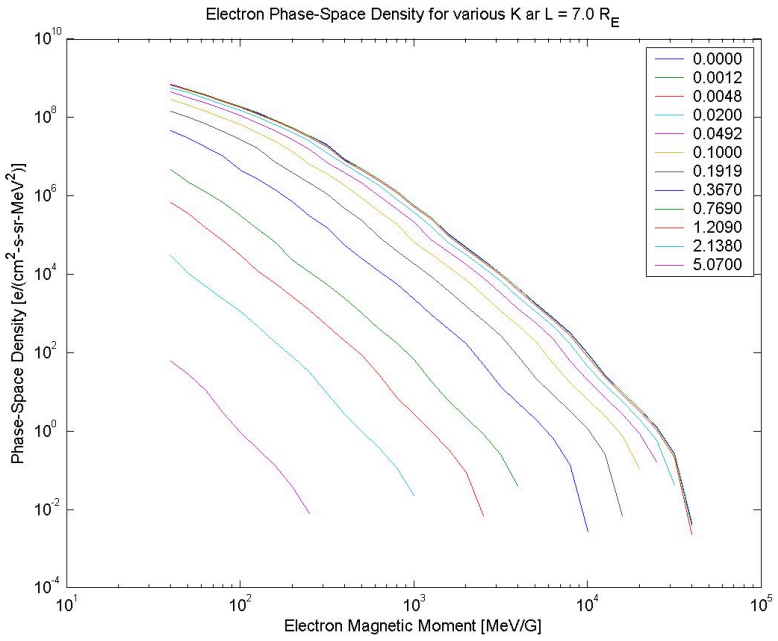

Figure A16. The same quantities as in Fig. A15 but in log-log format.

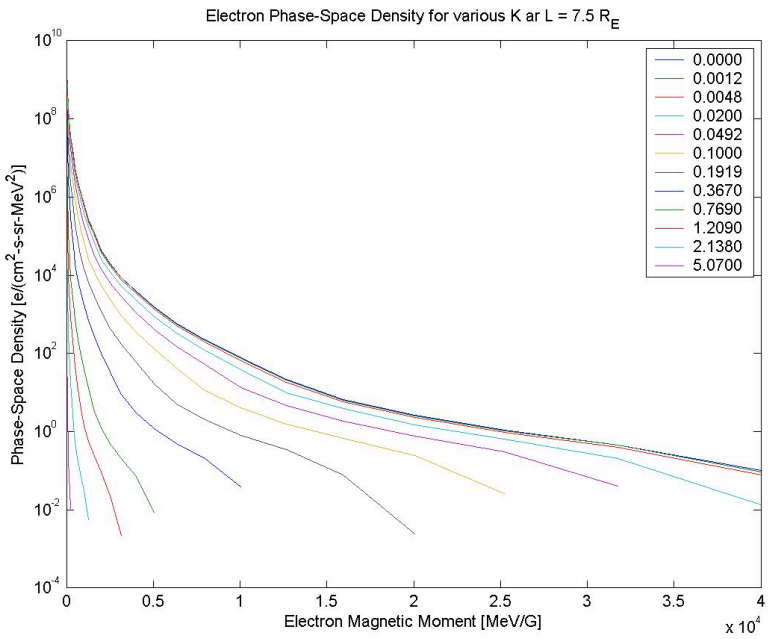

Figure A17. AE-8 phase-space density at L = 7.5 as functions of μ for twelve values of K.

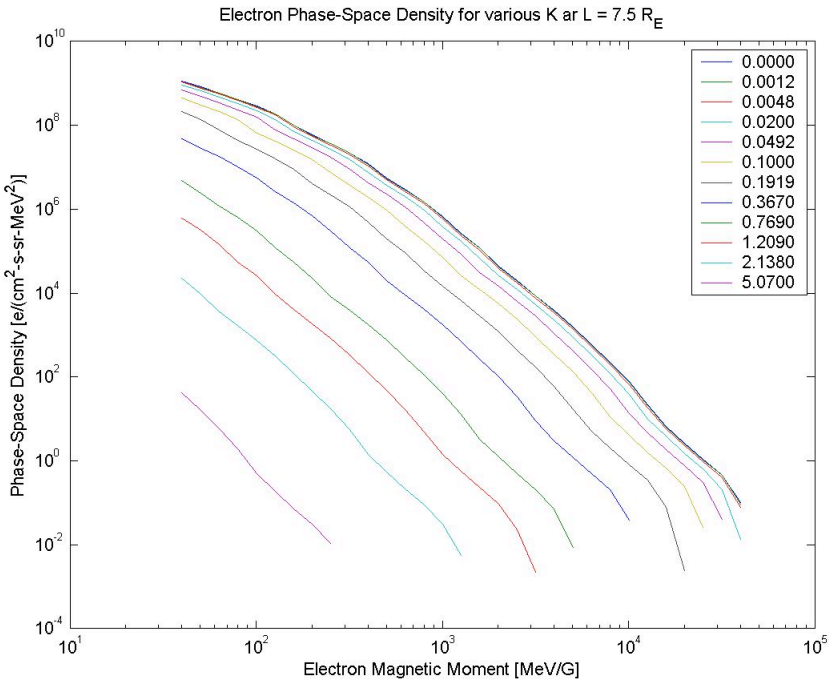

Figure A18. The same quantities as in Fig. A17 but in log-log format.

Appendix B: AE-8 Phase-Space Density as Functions of K

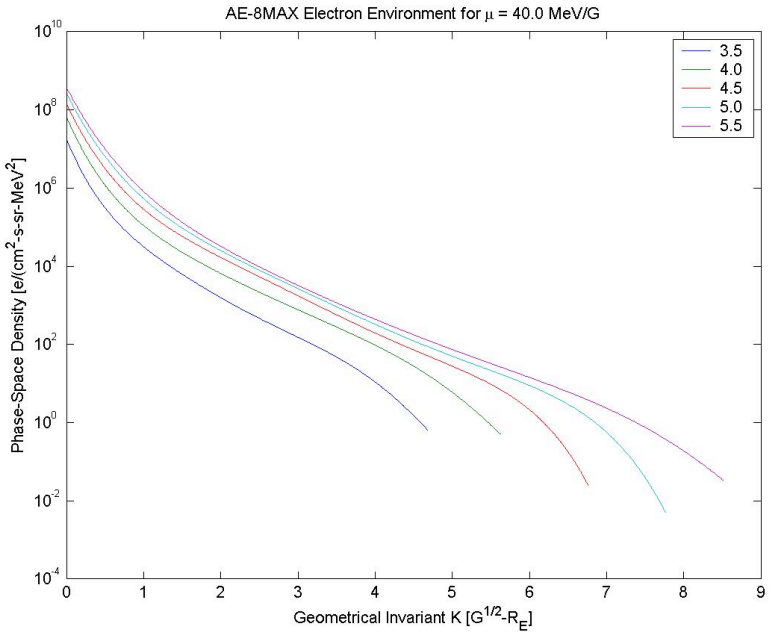

Figure B1a. AE-8 phase-space density in the inner region, 3.5 R_E < L < 5.5 R_E, as functions of K for fixed μ = 40.0 MeV/G.

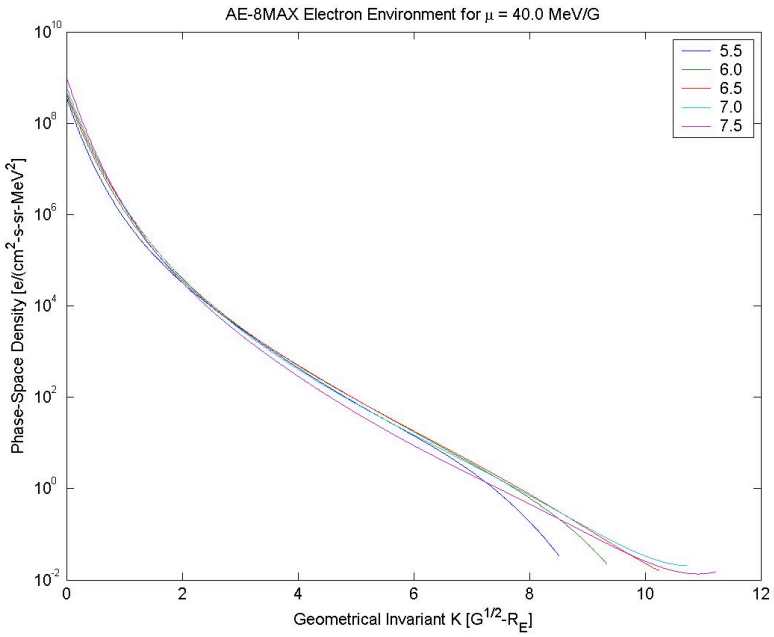

Figure B1b. AE-8 phase-space density in the outer region, 5.5 R_E < L < 7.5 R_E, as functions of K for fixed μ = 40.0 MeV/G.

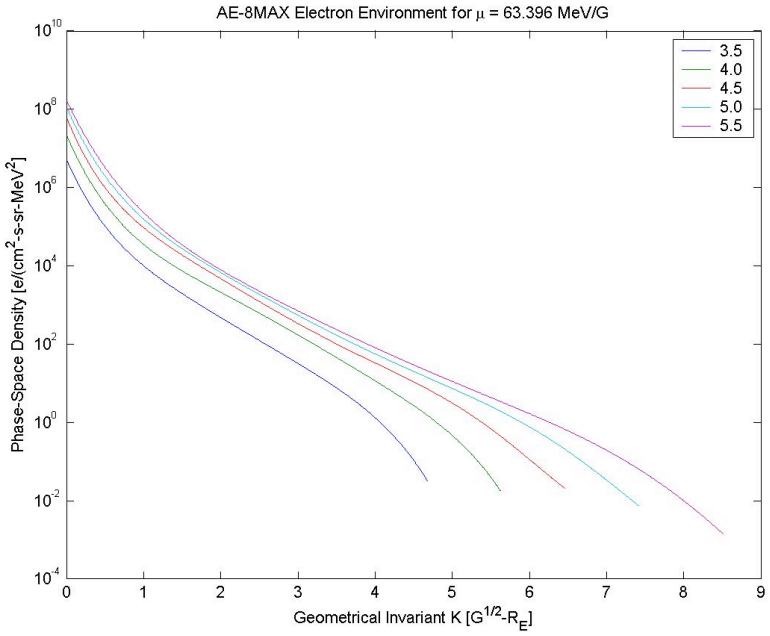

Figure B2a. AE-8 phase-space density in the inner region, 3.5 R_E < L < 5.5 R_E, as functions of K for fixed μ = 63.396 MeV/G.

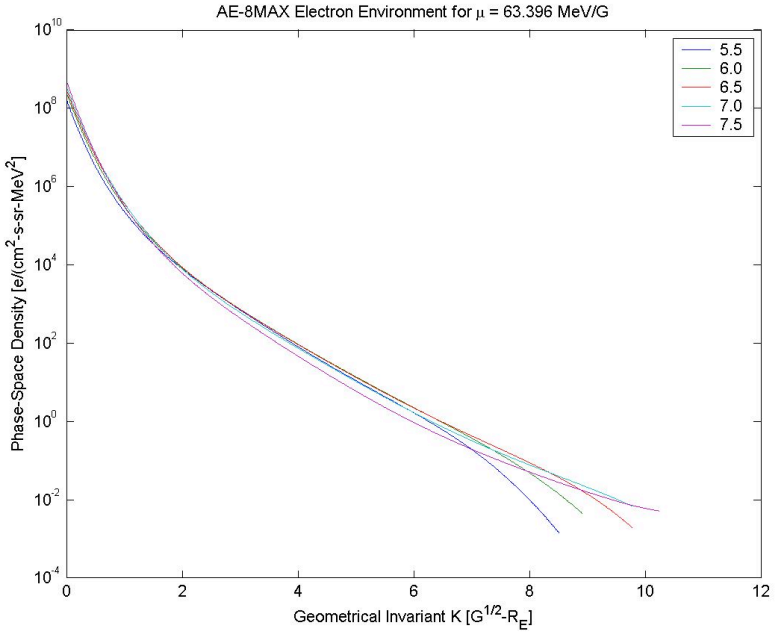

Figure B2b. AE-8 phase-space density in the outer region, 5.5 R_E < L < 7.5 R_E, as functions of K for fixed μ = 63.396 MeV/G.

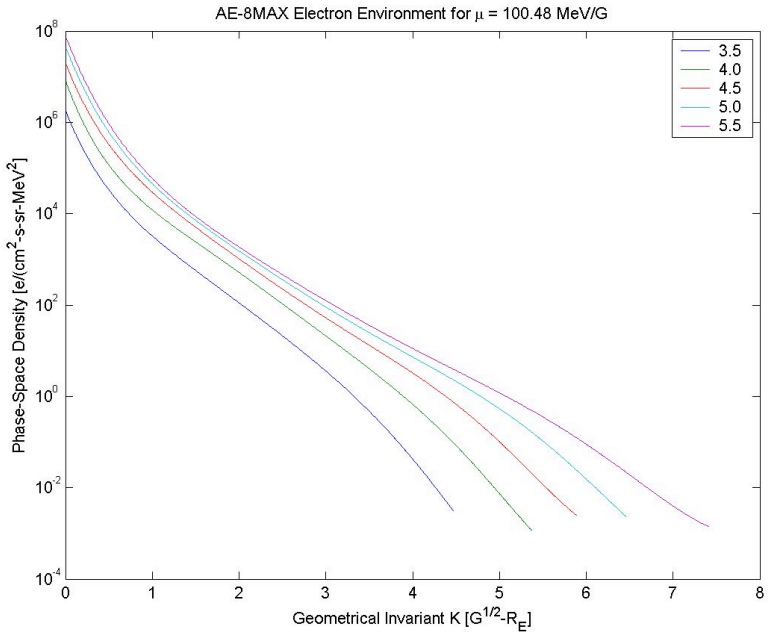

Figure B3a. AE-8 phase-space density in the inner region, 3.5 R_E < L < 5.5 R_E, as functions of K for fixed μ = 100.48 MeV/G.

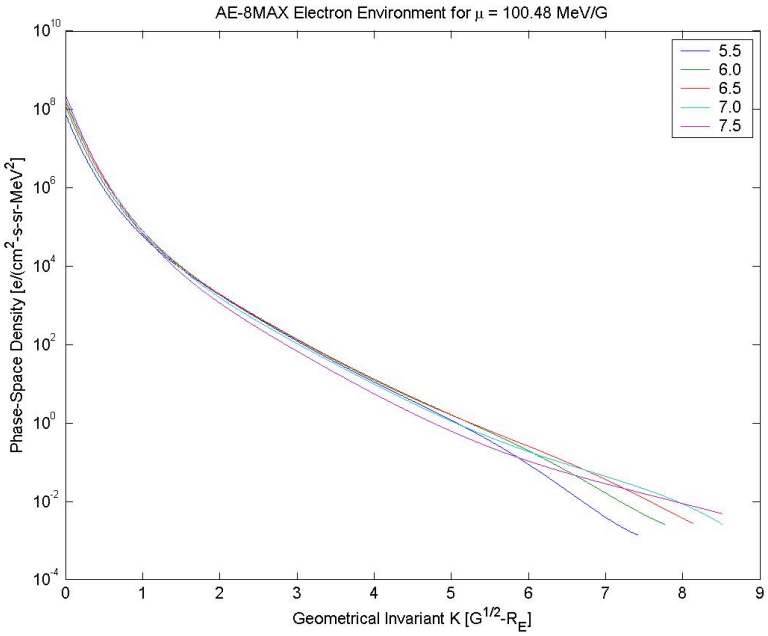

Figure B3b. AE-8 phase-space density in the outer region, 5.5 R_E < L < 7.5 R_E, as functions of K for fixed μ = 100.48 MeV/G.

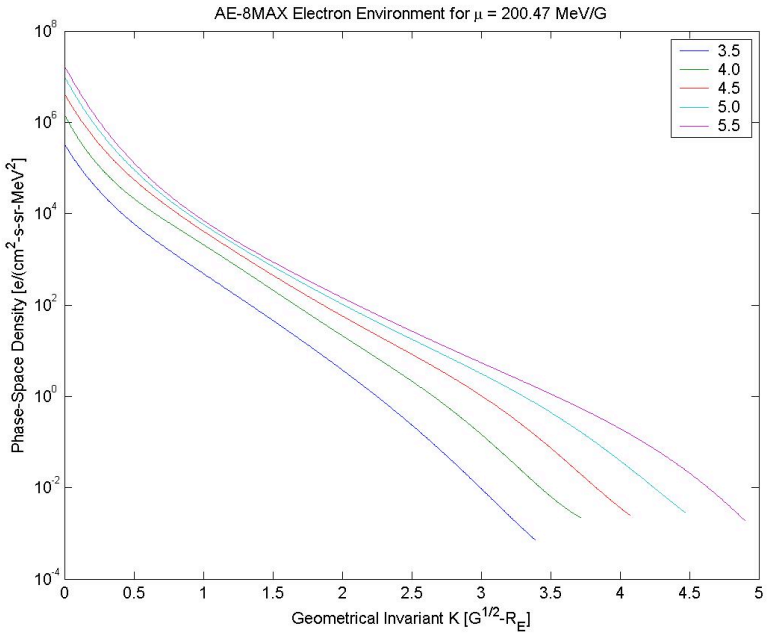

Figure B4a. AE-8 phase-space density in the inner region, 3.5 R_E < L < 5.5 R_E, as functions of K for fixed μ = 200.47 MeV/G.

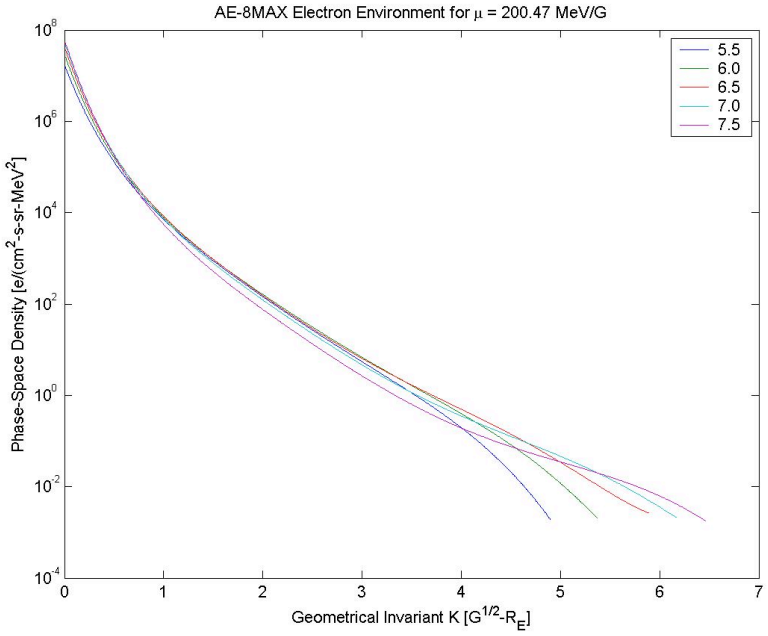

Figure B4b. AE-8 phase-space density in the outer region, 5.5 R_E < L < 7.5 R_E, as functions of K for fixed μ = 200.47 MeV/G.

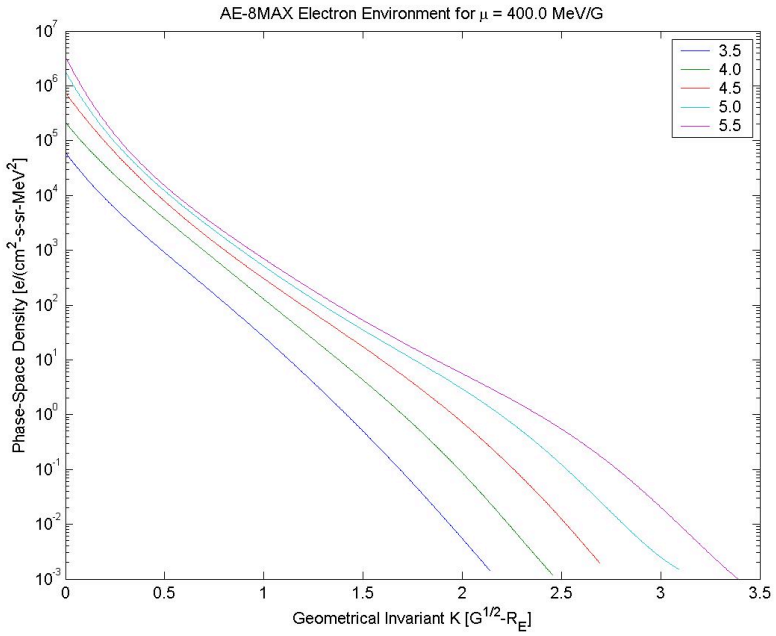

Figure B5a. AE-8 phase-space density in the inner region, 3.5 R_E < L < 5.5 R_E, as functions of K for fixed μ = 400.0 MeV/G.

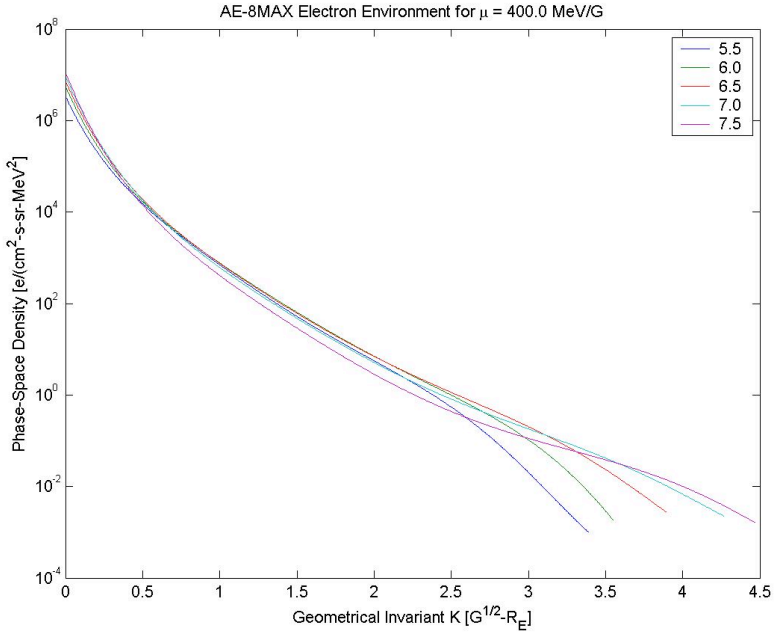

Figure B5b. AE-8 phase-space density in the outer region, 5.5 R_E < L < 7.5 R_E, as functions of K for fixed μ = 400.0 MeV/G.

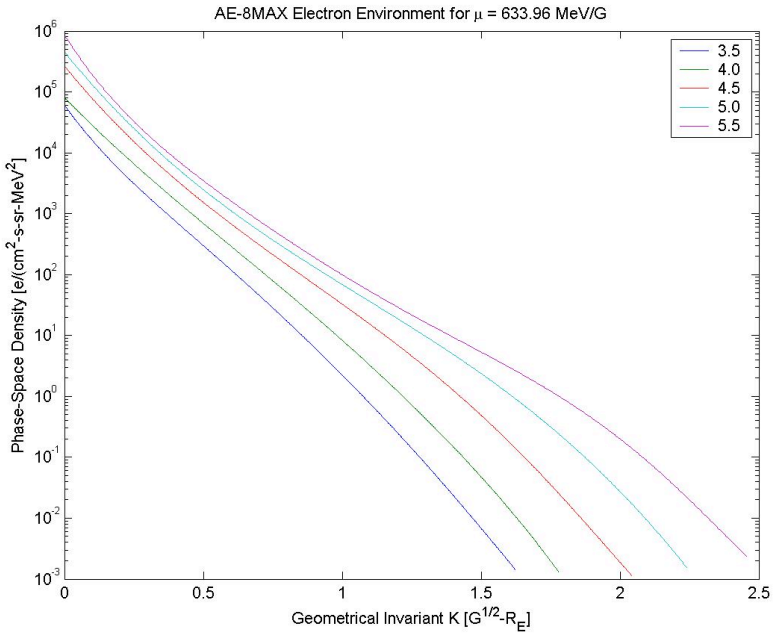

Figure B6a. AE-8 phase-space density in the inner region, 3.5 R_E < L < 5.5 R_E, as functions of K for fixed μ = 633.96 MeV/G.

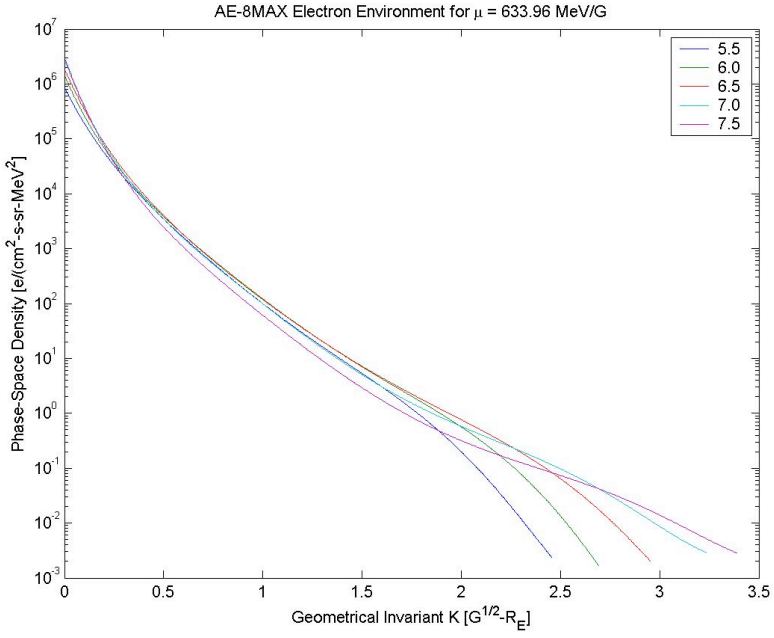

Figure B6b. AE-8 phase-space density in the outer region, 5.5 R_E < L < 7.5 R_E, as functions of K for fixed μ = 633.96 MeV/G.

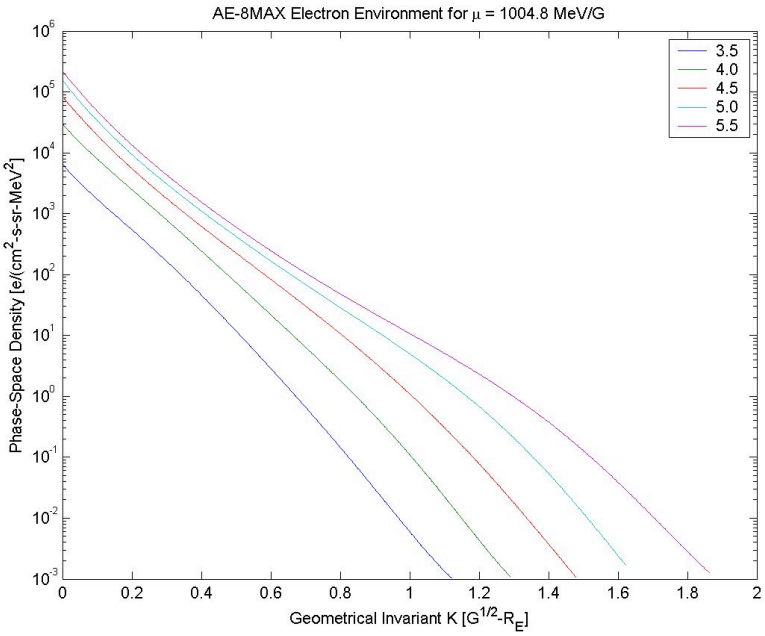

Figure B7a. AE-8 phase-space density in the inner region, 3.5 R_E < L < 5.5 R_E, as functions of K for fixed μ = 1004.8 MeV/G.

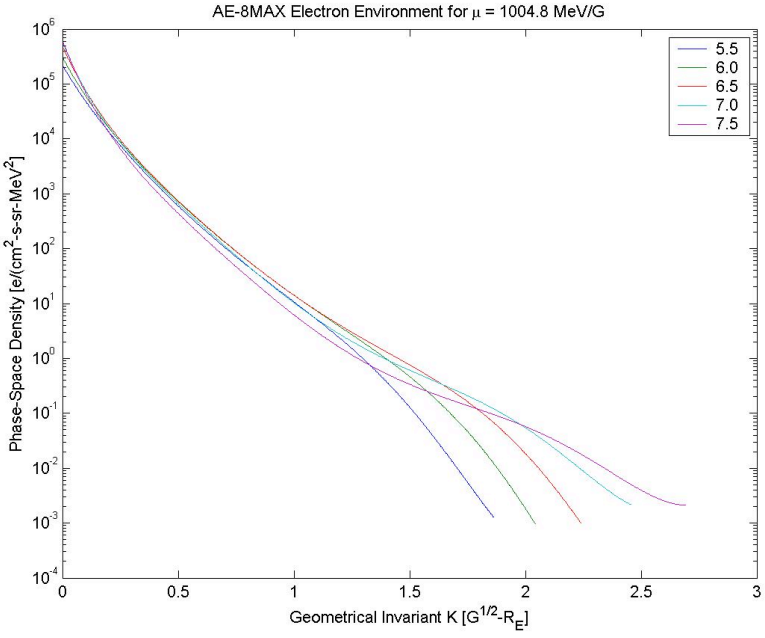

Figure B7b. AE-8 phase-space density in the outer region, 5.5 R_E < L < 7.5 R_E, as functions of K for fixed μ = 1004.8 MeV/G.

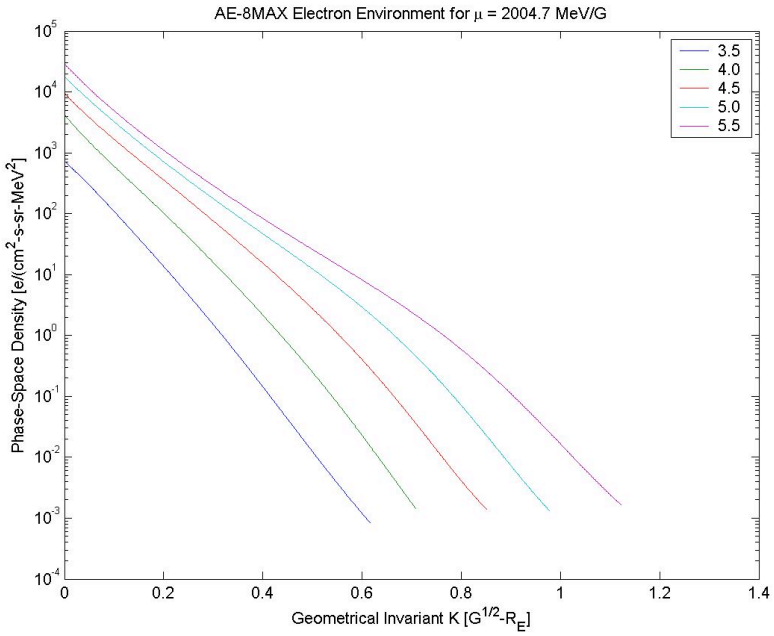

Figure B8a. AE-8 phase-space density in the inner region, 3.5 R_E < L < 5.5 R_E, as functions of K for fixed μ = 2004.7 MeV/G.

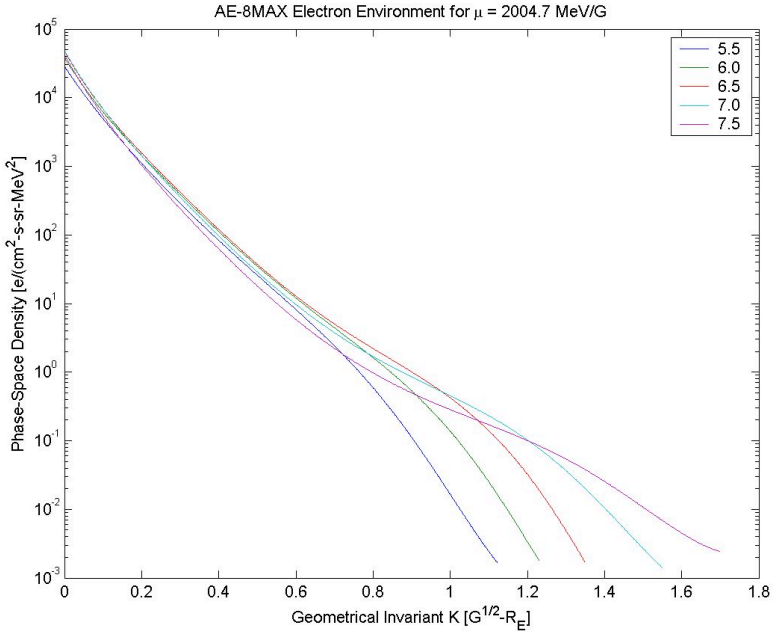

Figure B8b. AE-8 phase-space density in the outer region, 5.5 R_E < L < 7.5 R_E, as functions of K for fixed μ = 2004.7 MeV/G.

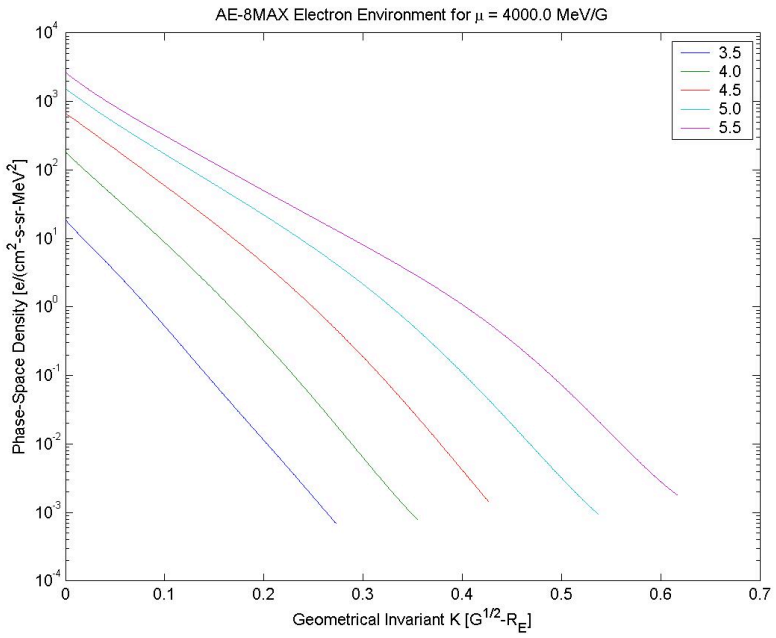

Figure B9a. AE-8 phase-space density in the inner region, 3.5 R_E < L < 5.5 R_E, as functions of K for fixed μ = 4000.0 MeV/G.

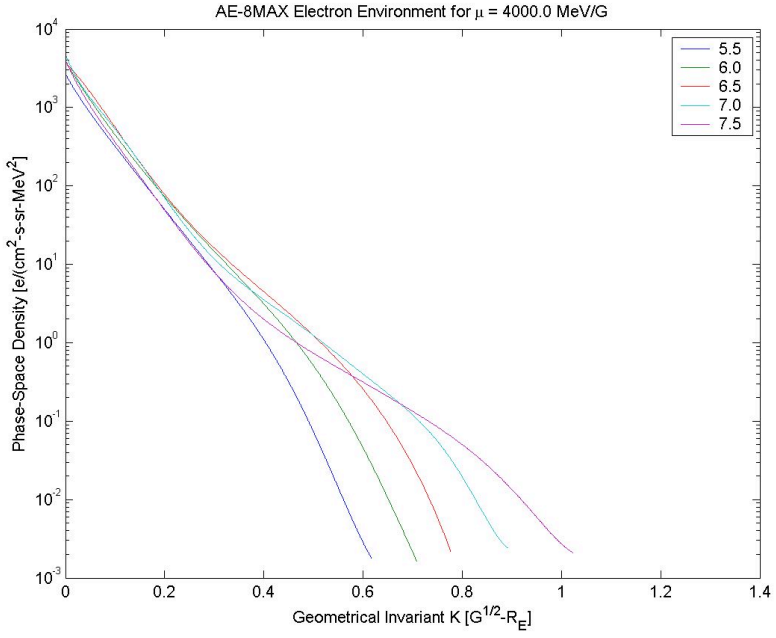

Figure B9b. AE-8 phase-space density in the outer region, 5.5 R_E < L < 7.5 R_E, as functions of K for fixed μ = 4000.0 MeV/G.

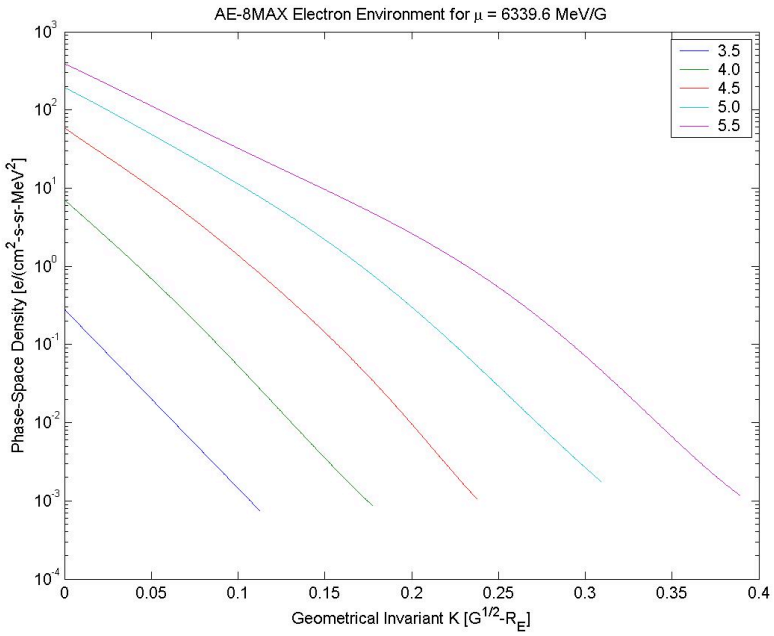

Figure B10a. AE-8 phase-space density in the inner region, 3.5 R_E < L < 5.5 R_E, as functions of K for fixed μ = 6339.6 MeV/G.

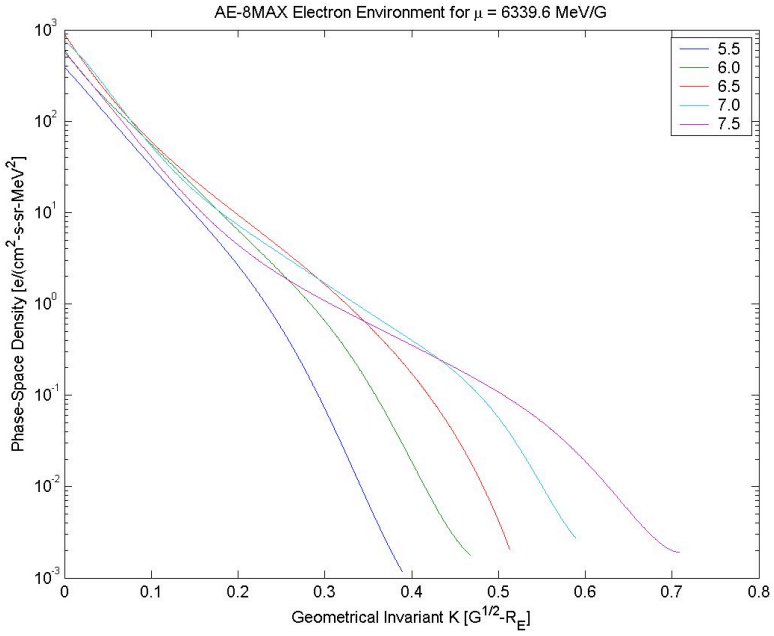

Figure B10b. AE-8 phase-space density in the outer region, 5.5 R_E < L < 7.5 R_E, as functions of K for fixed μ = 6339.6 MeV/G.

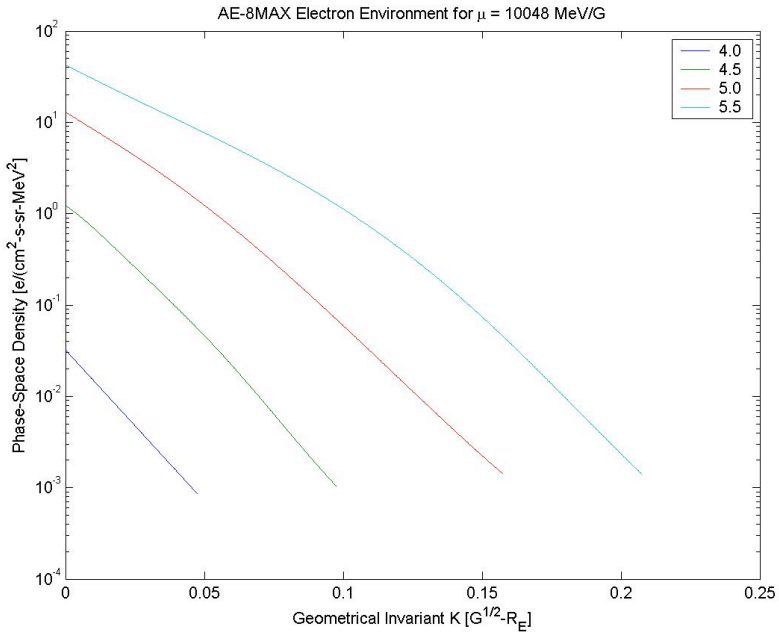

Figure B11a. AE-8 phase-space density in the inner region, 3.5 R_E < L < 5.5 R_E, as functions of K for fixed μ = 10048 MeV/G. No trapped electrons are seen at 3.5 R_E.

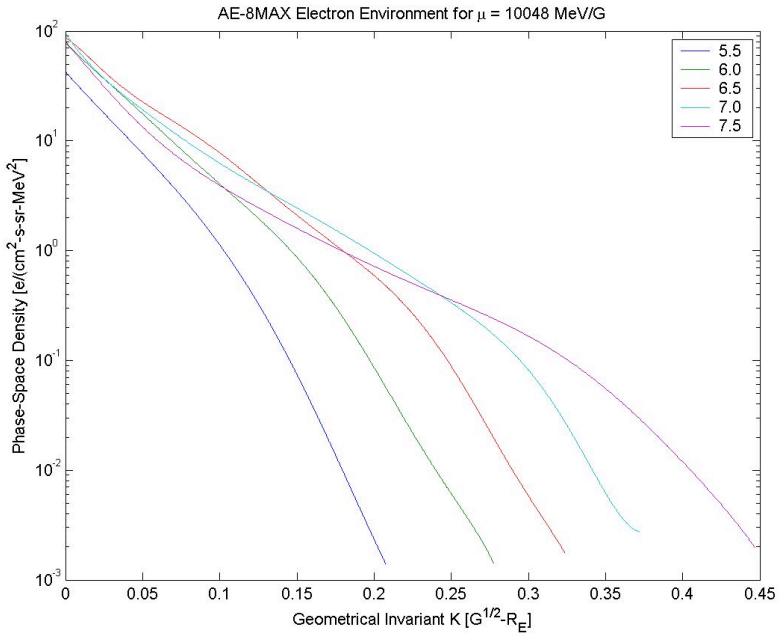

Figure B11b. AE-8 phase-space density in the outer region, 5.5 R_E < L < 7.5 R_E, as functions of K for fixed μ = 10048 MeV/G.

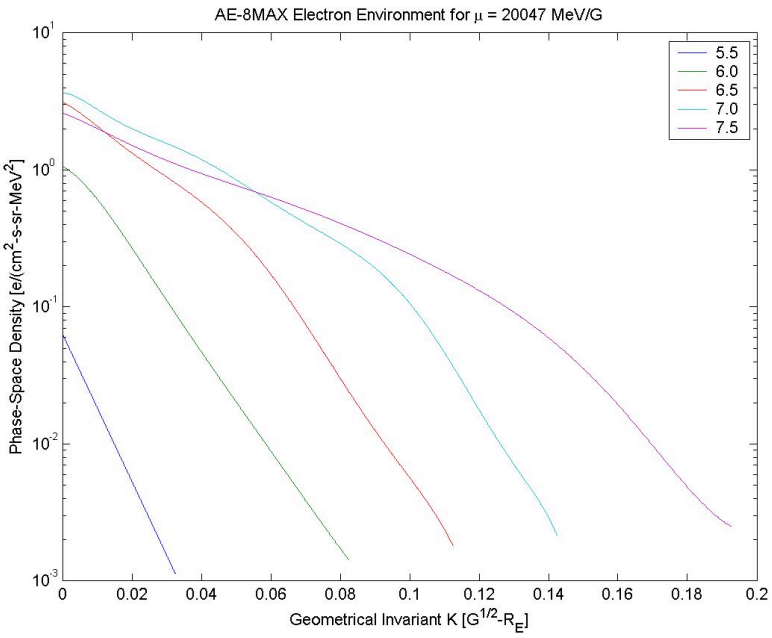

Figure B12. AE-8 phase-space density in the outer region, 5.5 R_E < L < 7.5 R_E, as functions of K for fixed μ = 20047 MeV/G. No trapped electrons are seen at and below L = 5.0 R_E.

Appendix C: AP-8 Phase-Space Density as Functions of μ

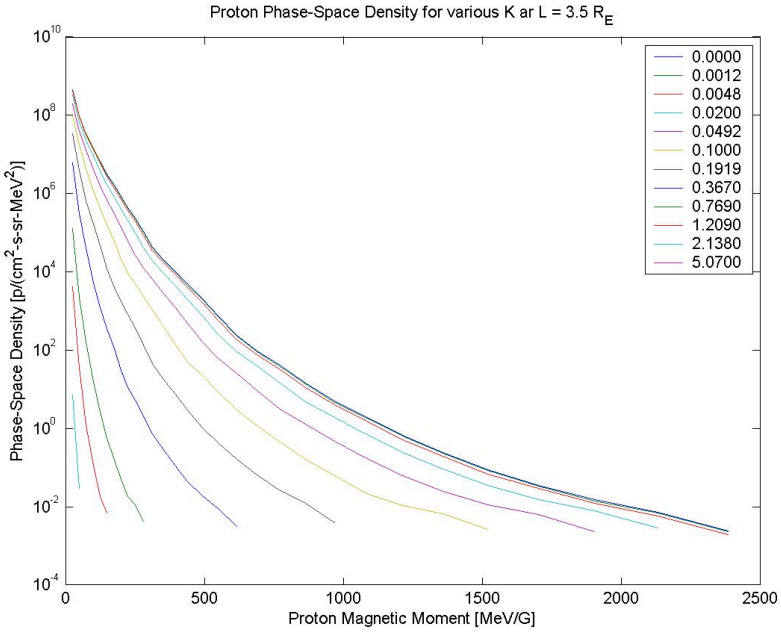

Figure C1. AP-8 phase-space density at L = 3.5 as functions of μ for twelve values of K.

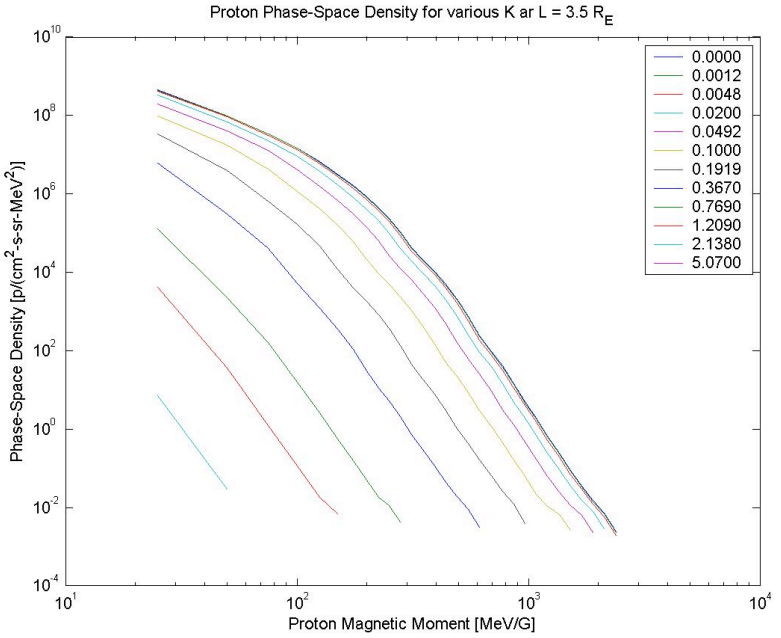

Figure C2. The same quantities as in Fig. C1 but in log-log format.

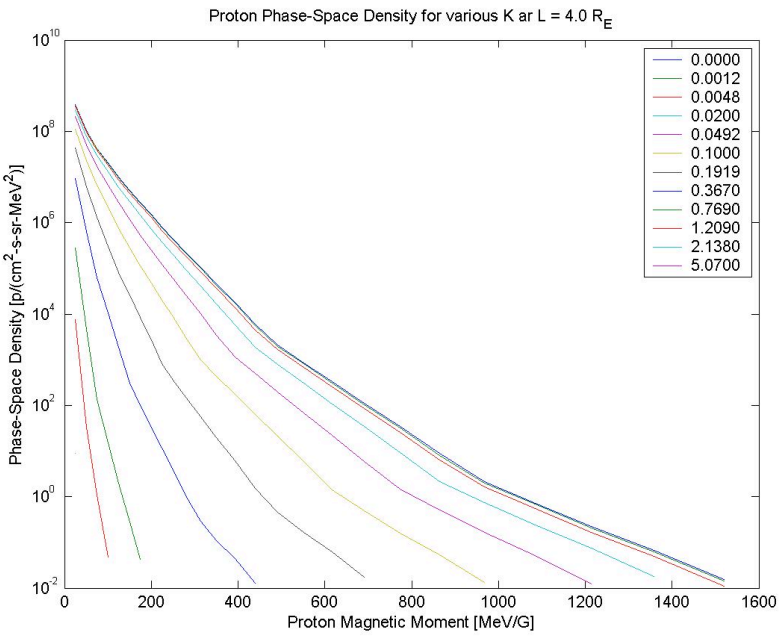

Figure C3. AP-8 phase-space density at L = 4.0 as functions of μ for twelve values of K.

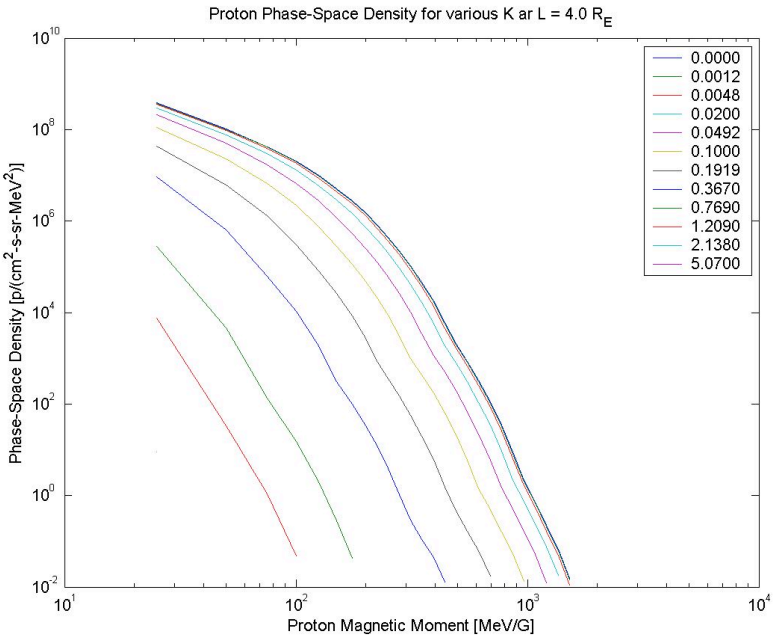

Figure C4. The same quantities as in Fig. C3 but in log-log format.

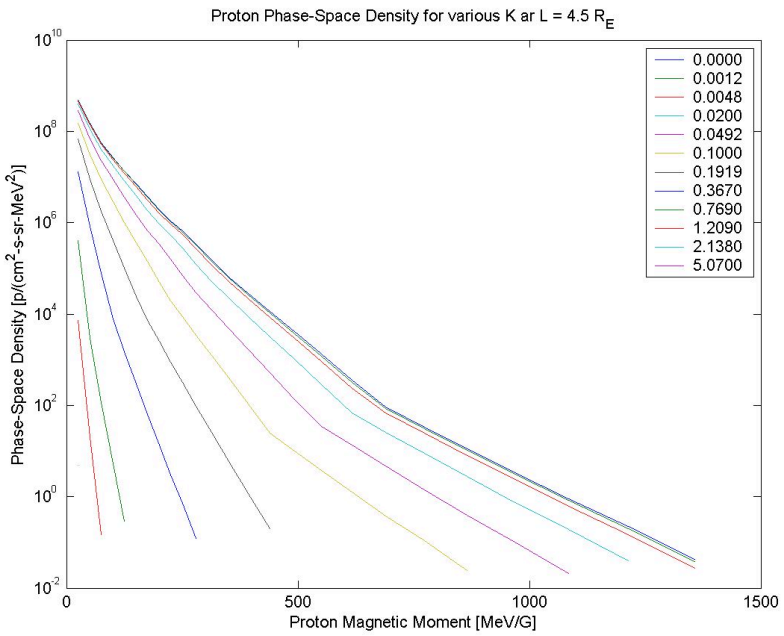

Figure C5. AP-8 phase-space density at L = 4.5 as functions of μ for twelve values of K.

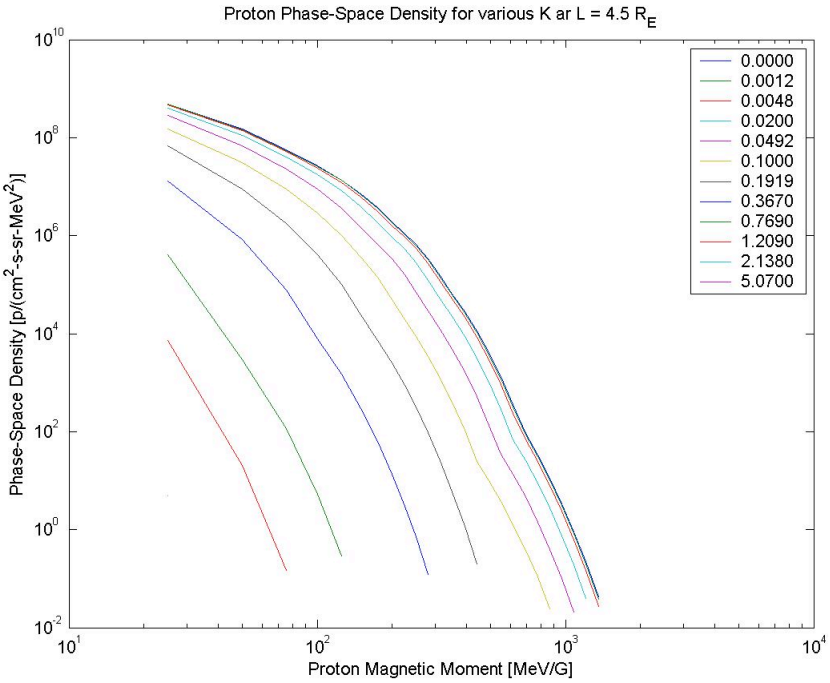

Figure C6. The same quantities as in Fig. C5 but in log-log format.

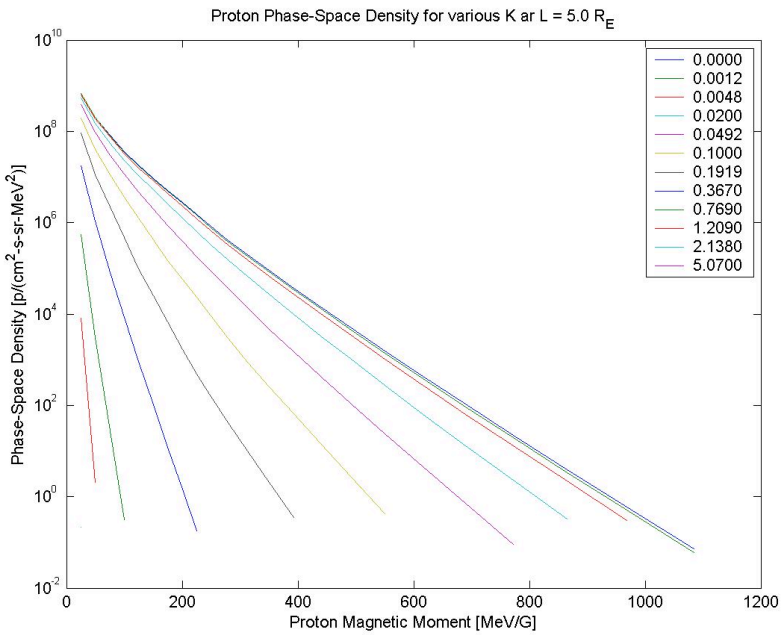

Figure C7. AP-8 phase-space density at L = 5.0 as functions of μ for twelve values of K.

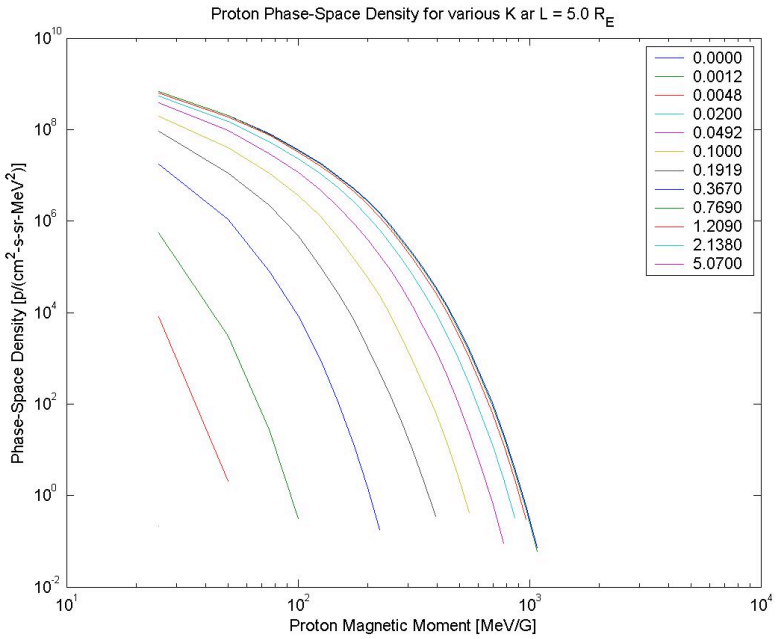

Figure C8. The same quantities as in Fig. C7 but in log-log format.

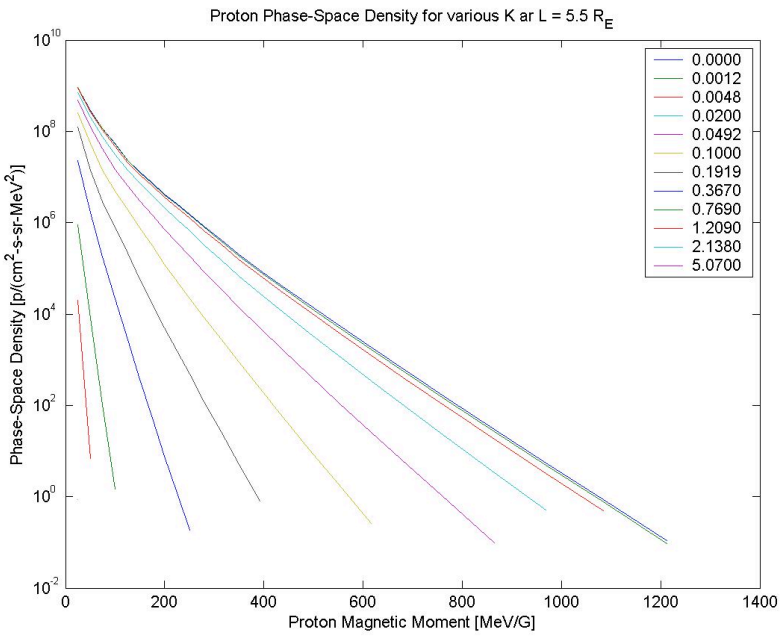

Figure C9. AP-8 phase-space density at L = 5.5 as functions of μ for twelve values of K.

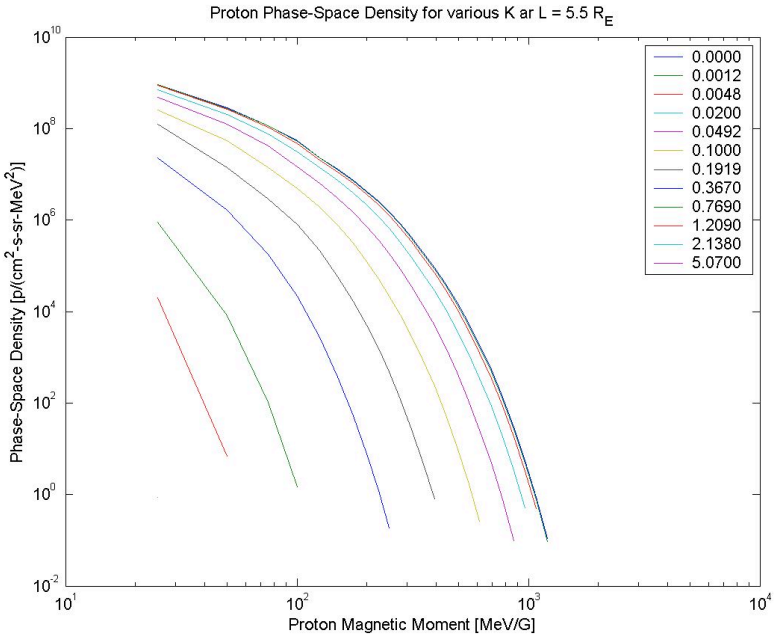

Figure C10. The same quantities as in Fig. C9 but in log-log format.

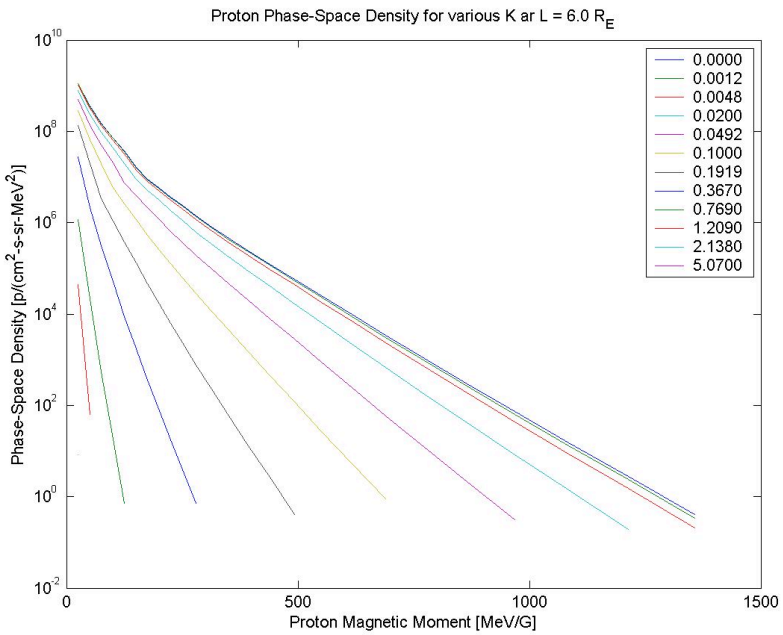

Figure C11. AP-8 phase-space density at L = 6.0 as functions of μ for twelve values of K.

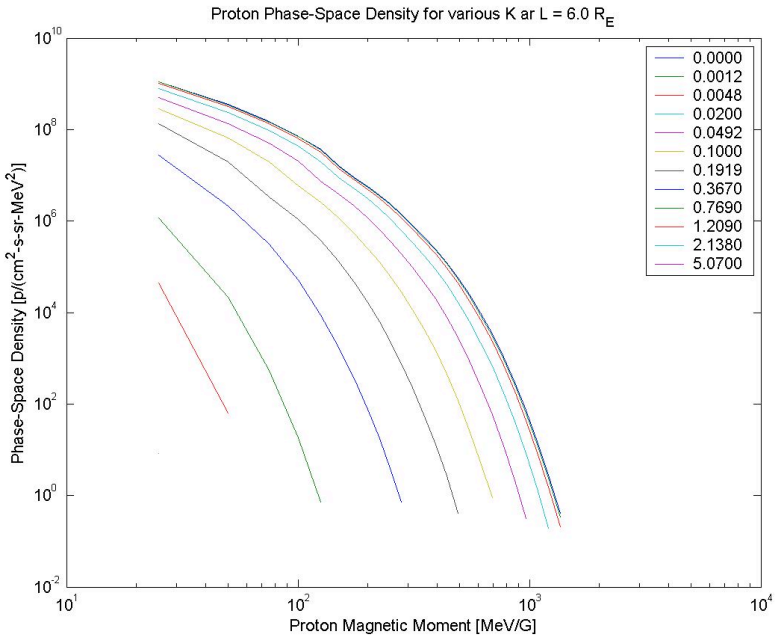

Figure C12. The same quantities as in Fig. C11 but in log-log format.

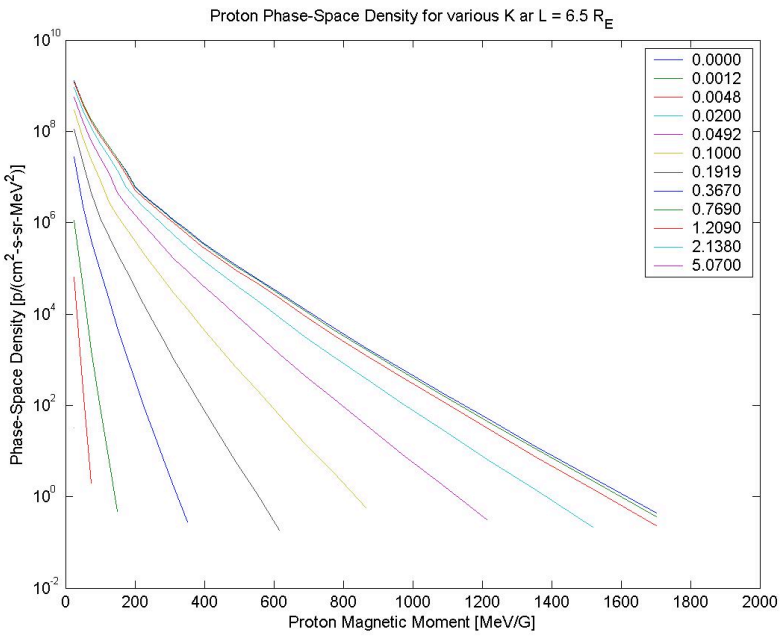

Figure C13. AP-8 phase-space density at L = 6.5 as functions of μ for twelve values of K.

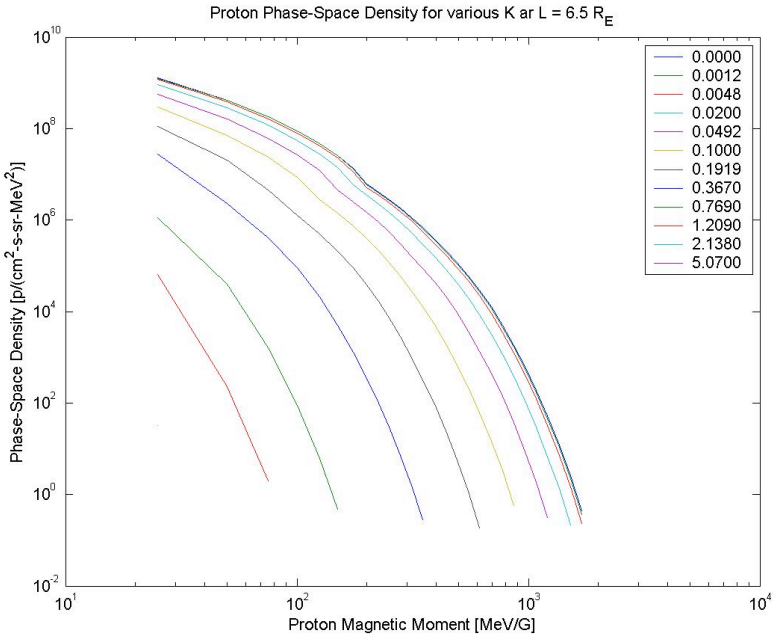

Figure C14. The same quantities as in Fig. C13 but in log-log format.

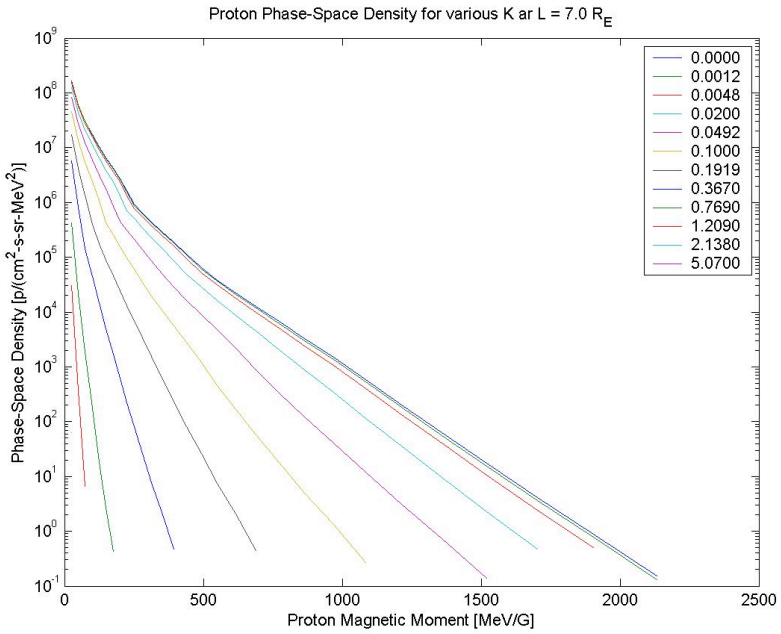

Figure C15. AP-8 phase-space density at L = 7.0 as functions of μ for twelve values of K.

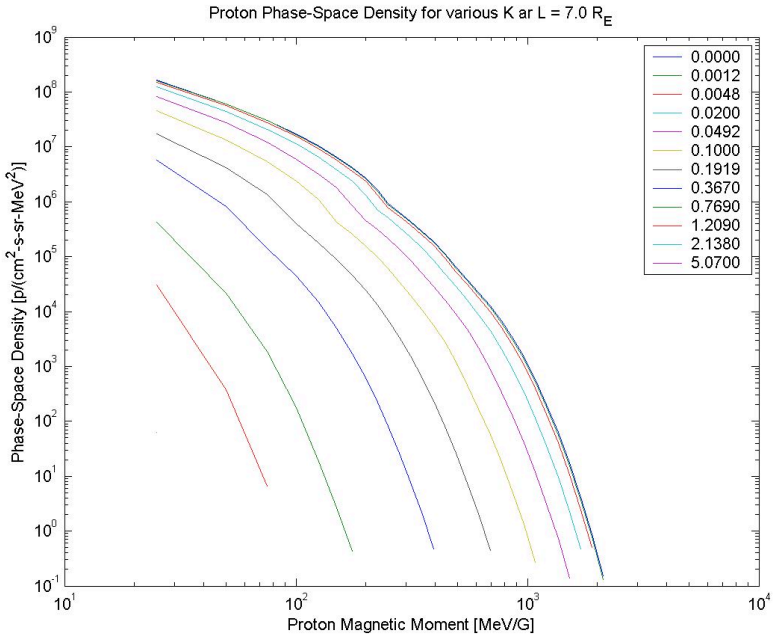

Figure C16. The same quantities as in Fig. C15 but in log-log format.

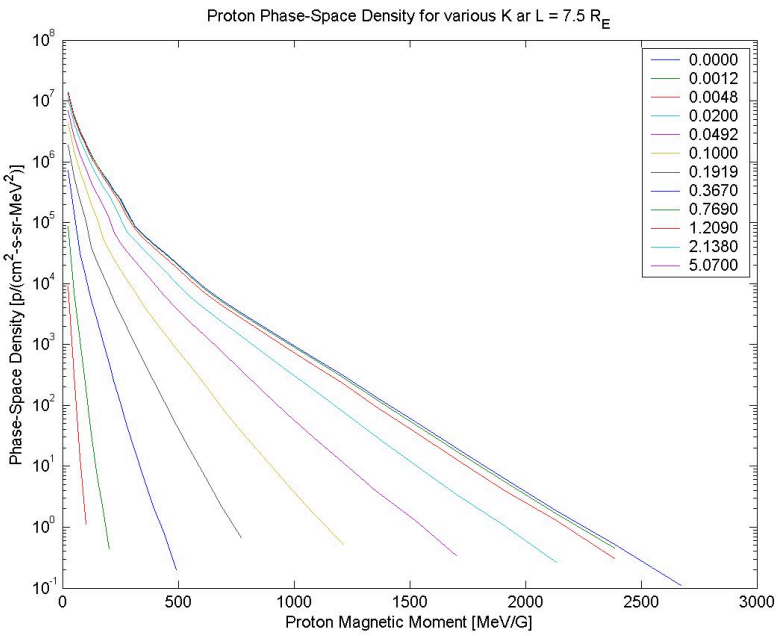

Figure C17. AP-8 phase-space density extrapolated to L = 7.5 as functions of μ for twelve values of K.

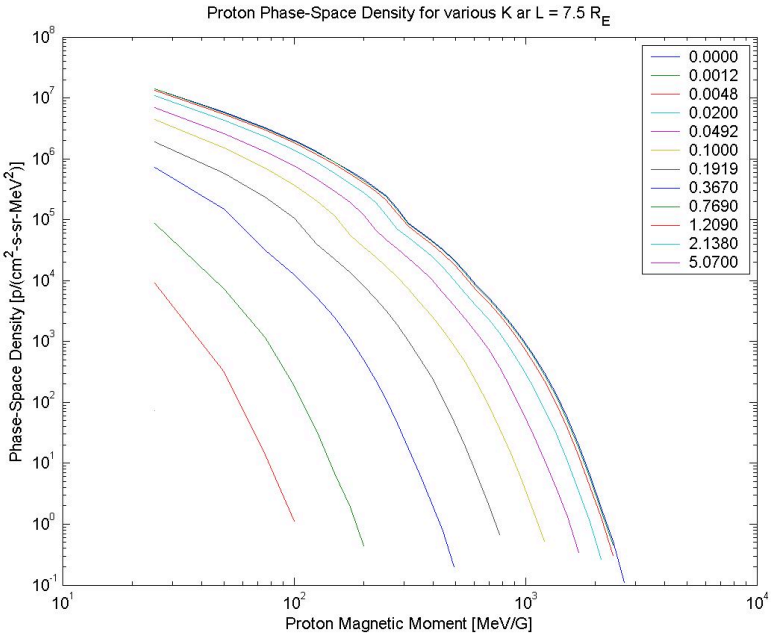

Figure C18. The same quantities as in Fig. C17 but in log-log format.

Appendix D: AP-8 Phase-Space Density as Functions of K

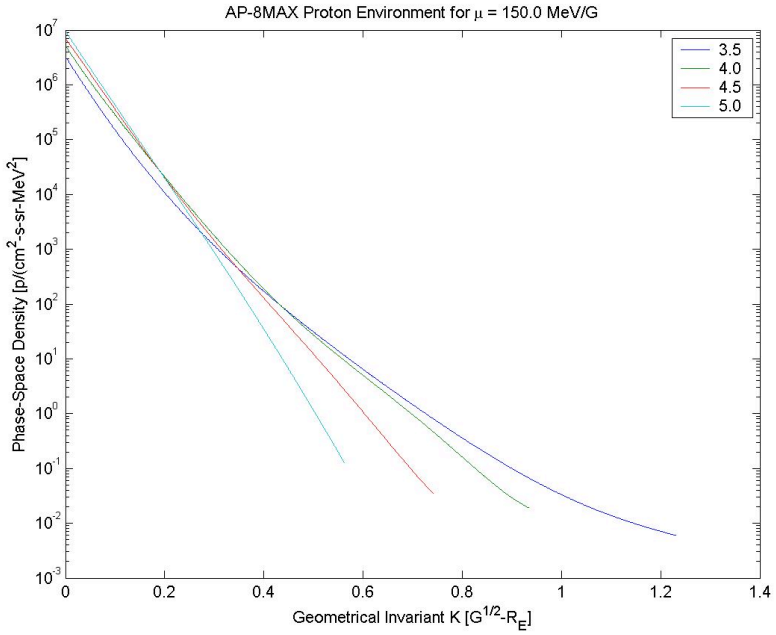

Figure D1a. AP-8 phase-space density in the inner region, 3.5 R_E < L < 5.0 R_E, as functions of K for fixed μ = 150.0 MeV/G.

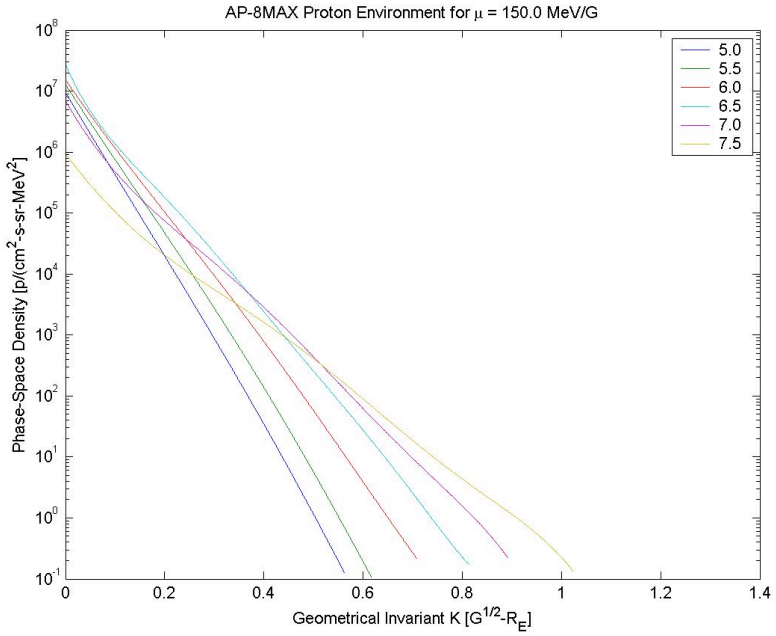

Figure D1b. AP-8 phase-space density in the outer region, 5.0 R_E < L < 7.5 R_E, as functions of K for fixed μ = 150.0 MeV/G (curve labeled 7.5 R_E is an extrapolation).

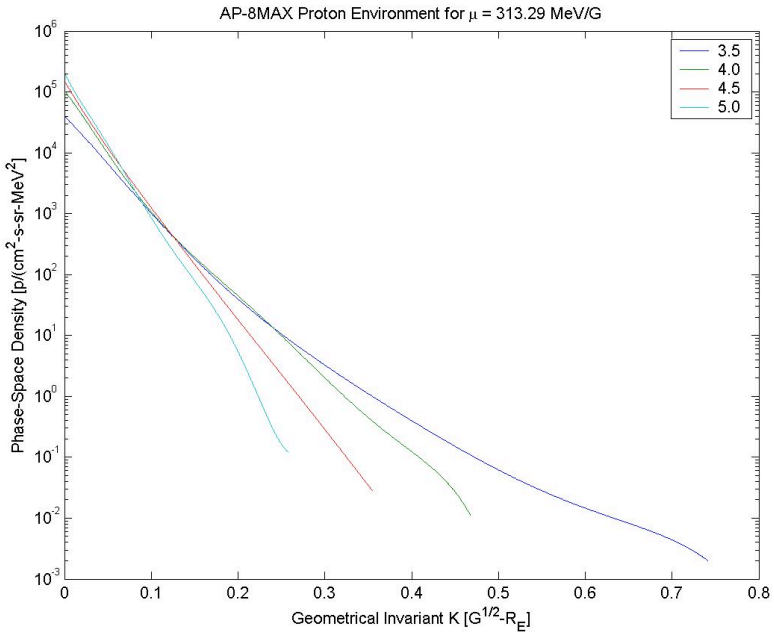

Figure D2a. AP-8 phase-space density in the inner region, 3.5 R_E < L < 5.0 R_E, as functions of K for fixed μ = 313.29 MeV/G.

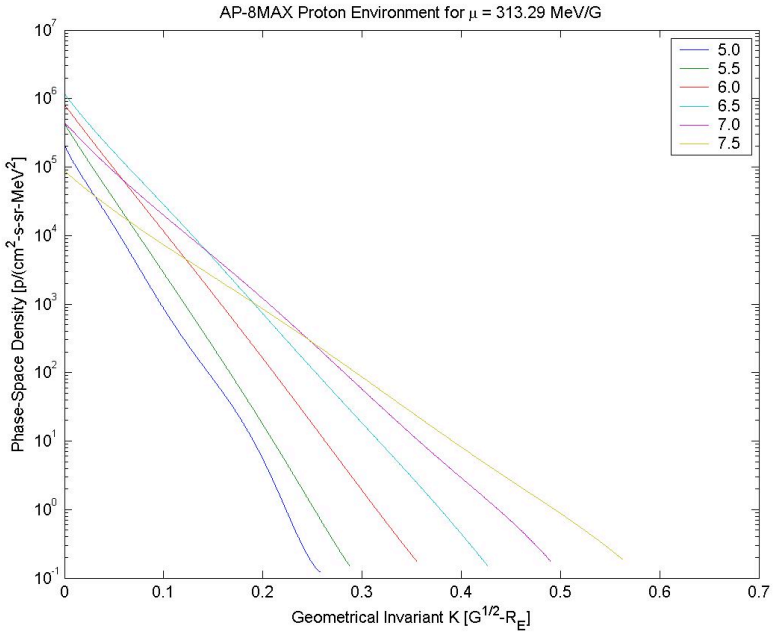

Figure D2b. AP-8 phase-space density in the outer region, 5.0 R_E < L < 7.5 R_E, as functions of K for fixed μ = 313.29 MeV/G (curve labeled 7.5 R_E is an extrapolation).

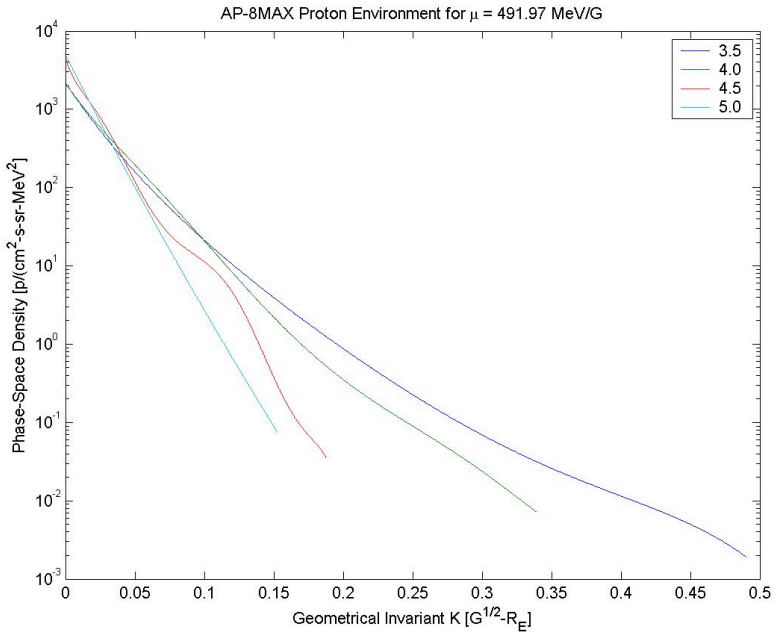

Figure D3a. AP-8 phase-space density in the inner region, 3.5 R_E < L < 5.0 R_E, as functions of K for fixed μ = 491.97 MeV/G.

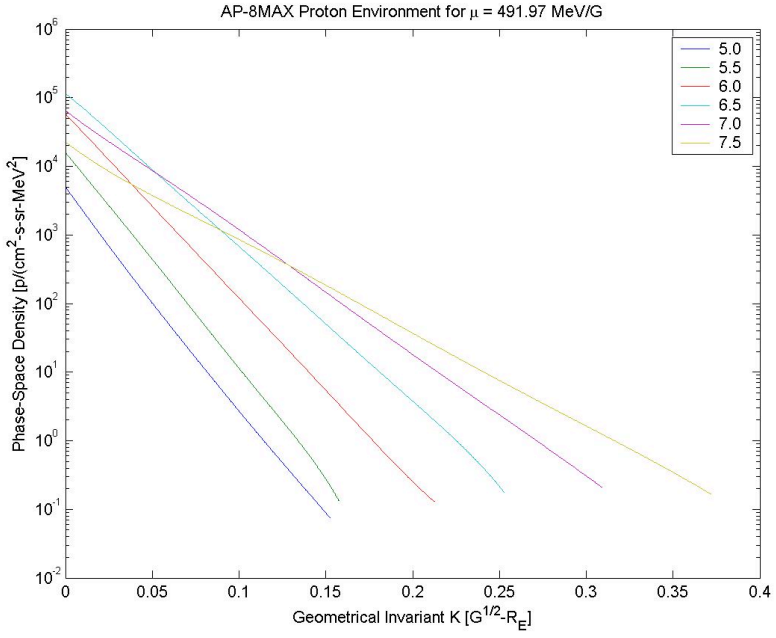

Figure D3b. AP-8 phase-space density in the outer region, 5.0 R_E < L < 7.5 R_E, as functions of K for fixed μ = 491.97 MeV/G(curve labeled 7.5 R_E is an extrapolation).

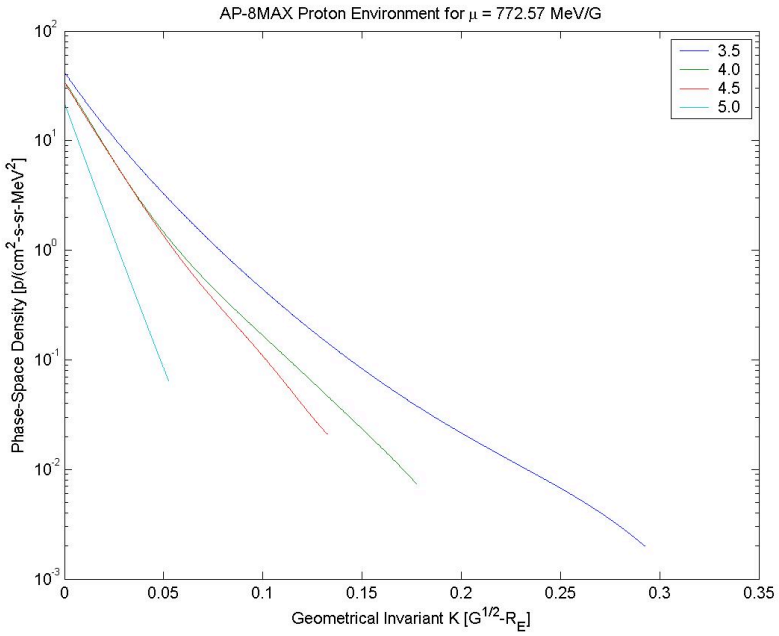

Figure D4a. AP-8 phase-space density in the inner region, 3.5 R_E < L < 5.0 R_E, as functions of K for fixed μ = 772.57 MeV/G.

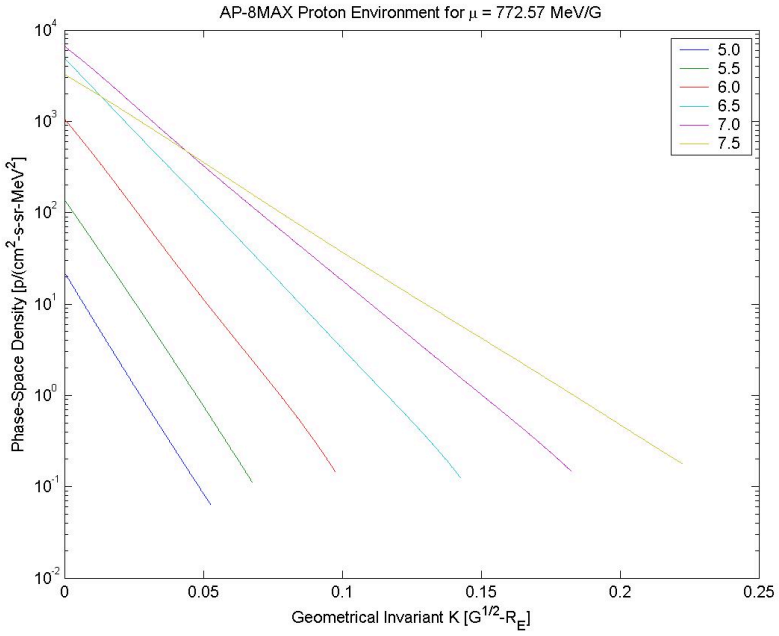

Figure D4b. AP-8 phase-space density in the outer region, 5.0 R_E < L < 7.5 R_E, as functions of K for fixed μ = 772.57 MeV/G (curve labeled 7.5 R_E is an extrapolation).

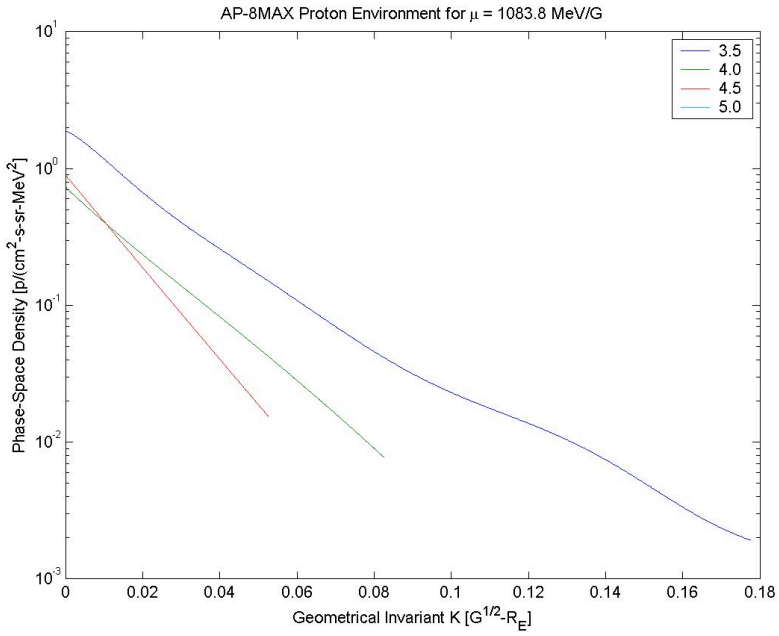

Figure D5a. AP-8 phase-space density in the inner region, 3.5 R_E < L < 5.0 R_E, as functions of K for fixed μ = 1083.8 MeV/G. Trapped protons vanish at L = 5 R_E.

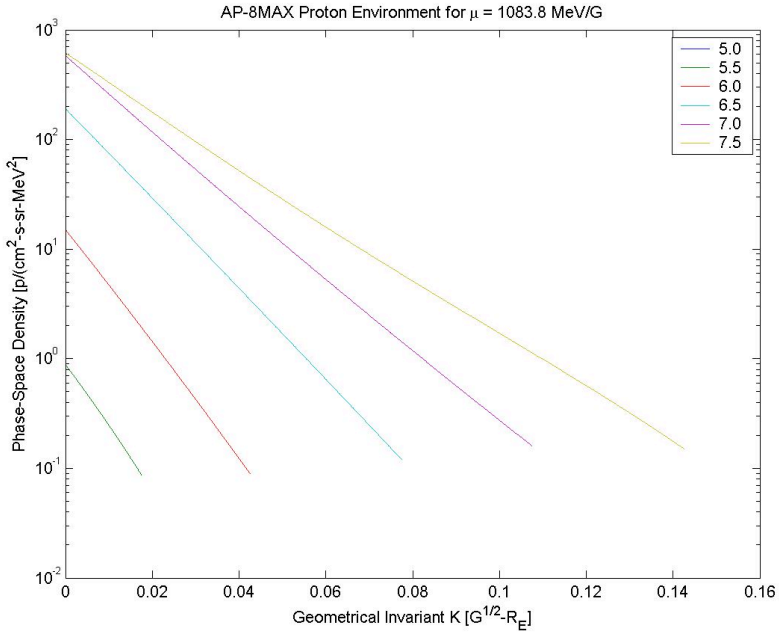

Figure D5b. AE-8 phase-space density in the outer region, 5.0 R_E < L < 7.5 R_E, as functions of K, for fixed μ = 1083.8 MeV/G. Trapped protons vanish at L = 5 R_E (curve labeled 7.5 R_E is an extrapolation).

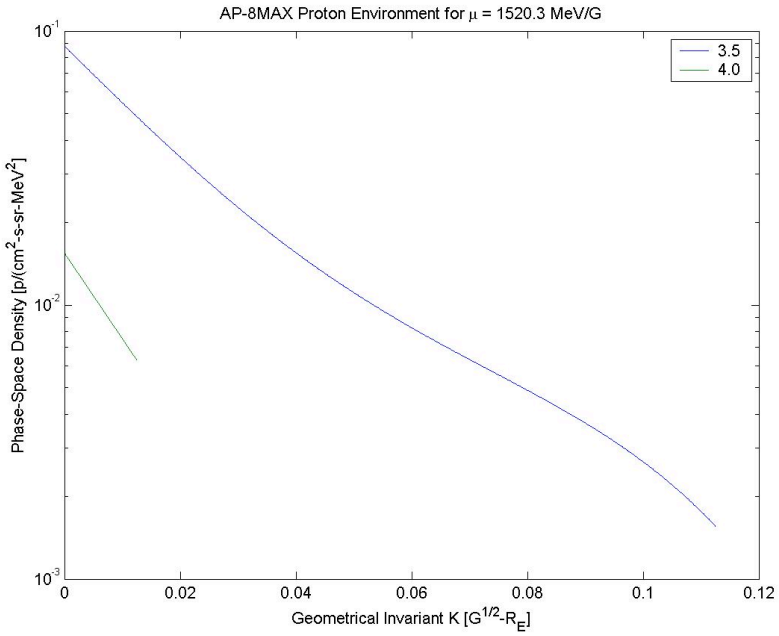

Figure D6a. AP-8 phase-space density in the inner region, 3.5 R_E < L < 5.0 R_E, as functions of K for fixed μ = 1520.3 MeV/G. Trapped protons vanish beyond L = 4.0 R_E.

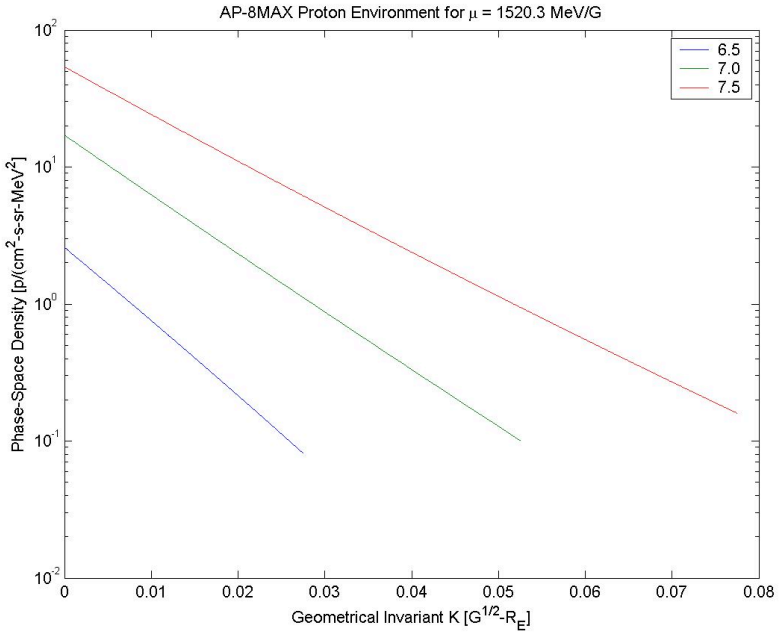

Figure D6b. AP-8 phase-space density in the outer region, 5.0 R_E < L < 7.5 R_E, as functions of K for fixed μ = 1520.3 MeV/G. Trapped protons vanish within L = 6.5 R_E (curve labeled 7.5 R_E is an extrapolation).


Los Alamos
NATIONAL LABORATORY
EST. 1943